

**NLFEA of one-way slabs in transition between shear and punching
Recommendations for modeling**

de Sousa, Alex M.D.; Lantsoght, Eva O.L.; Genikomsou, Aikaterini S.; Prado, Lisiane P.; El Debs, Mounir K.

DOI

[10.1016/j.engstruct.2023.116617](https://doi.org/10.1016/j.engstruct.2023.116617)

Publication date

2023

Document Version

Final published version

Published in

Engineering Structures

Citation (APA)

de Sousa, A. M. D., Lantsoght, E. O. L., Genikomsou, A. S., Prado, L. P., & El Debs, M. K. (2023). NLFEA of one-way slabs in transition between shear and punching: Recommendations for modeling. *Engineering Structures*, 293, Article 116617. <https://doi.org/10.1016/j.engstruct.2023.116617>

Important note

To cite this publication, please use the final published version (if applicable).
Please check the document version above.

Copyright

Other than for strictly personal use, it is not permitted to download, forward or distribute the text or part of it, without the consent of the author(s) and/or copyright holder(s), unless the work is under an open content license such as Creative Commons.

Takedown policy

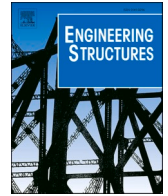
Please contact us and provide details if you believe this document breaches copyrights.
We will remove access to the work immediately and investigate your claim.

Green Open Access added to TU Delft Institutional Repository

'You share, we take care!' - Taverne project

<https://www.openaccess.nl/en/you-share-we-take-care>

Otherwise as indicated in the copyright section: the publisher is the copyright holder of this work and the author uses the Dutch legislation to make this work public.



NLFEA of one-way slabs in transition between shear and punching: Recommendations for modeling

Alex M.D. de Sousa^{a,*}, Eva O.L. Lantsoght^{b,c}, Aikaterini S. Genikomsou^d, Lisiane P. Prado^e, Mounir K. El Debs^f

^a University of São Paulo, São Carlos School of Engineering, São Carlos, Brazil

^b Politécnico, Universidad San Francisco de Quito, Quito, Ecuador

^c Delft University of Technology, Delft, the Netherlands

^d Queen's University, Ontario, Canada

^e São Paulo State University (UNESP), Guaratinguetá Campus, Brazil

^f University of São Paulo, São Carlos School of Engineering, São Carlos, Brazil

ARTICLE INFO

Keywords:

non-linear finite element analyses (NLFEA)

Shear capacity

Punching shear capacity^a

Modeling choices

ABSTRACT

Several studies investigated the precision of non-linear finite element analyses (NLFEA) to predict the shear capacity of beams or the punching capacity of slab-column connections. However, in the literature, there is little discussion regarding the results of NLFEA to predict the ultimate capacity and failure mechanism of slabs susceptible to different failure mechanisms. In this study, a set of tests from literature that developed different shear failure mechanisms was evaluated by NLFEA. A total of thirteen slabs were modeled, where slab's width and shear span varied. A coupled damaged-plasticity model was employed to simulate the concrete behavior. The proposed model was calibrated to simulate specimens that failed as wide beams in one-way shear and specimens that failed by punching shear. Besides, the effect of different modeling choices was investigated: (i) the assumed stress-strain behavior in compression; (ii) tensile stress-strain behavior; (iii) the inclusion or not of damage parameters and (iv) the viscosity parameter. The results indicated that, on average, the proposed modeling strategy represented the failure mechanism and ultimate loads well. Also, the same calibrated model was found capable of representing one-way shear failure and punching shear failure or mixed modes. The sensitivity study demonstrated that the tensile stress-strain behavior and viscosity parameter influences the results of the numerical models more significantly than the assumed stress-strain behavior in compression or including/not including the damage parameters. This paper concludes that modeling strategies during the calibration process shall be checked carefully before performing any parametric analyses to identify the accuracy of the numerical models to represent the different failure mechanisms. Moreover, the validation step of the modeling strategy shall identify possible limits of the numerical model to be considered in the parametric analyses.

1. Introduction

One-way slabs under large concentrated loads are commonly found in bridge deck slabs, industrial floor slabs and even residential buildings during their building or use [1–4]. Assuming the use of such structures on bridge deck slabs, the load position varies significantly during its use. In practice, different shear failure mechanisms may be critical for a given slab depending on the load position and other parameters, such as the slab width [5,6]. For instance, when the slab's width is not so large compared to the load size in the width direction, the slab may fail as a wide beam in one-way shear [7–10]. At the same time, when the load is

placed close to the support and the slab width is considerably larger than the load size, not the entire slab strip may contribute effectively to the sectional shear capacity [7]. In such cases, a slab strip called effective shear width is assumed to contribute effectively to the sectional shear capacity [1]. On the other hand, when the distance from the load to the support increases, the shear flow around the load becomes predominantly radial; hence, the punching failure may become more critical than a wide beam in one-way shear. In such cases, the sectional shear capacity may eventually not be reached if the test fails by punching.

Many studies contributed to predicting the sectional shear capacity of reinforced concrete (RC) beams [11,12] and the punching capacity of flat slabs or slab-column connections [13,14] using three-dimensional

* Corresponding author.

E-mail address: alex_dantas@usp.br (A.M.D. de Sousa).

<https://doi.org/10.1016/j.engstruct.2023.116617>

Received 22 March 2023; Received in revised form 30 May 2023; Accepted 15 July 2023

Available online 25 July 2023

0141-0296/© 2023 Elsevier Ltd. All rights reserved.

| Notations | | | |
|--------------|---|---------------------------|---|
| a | shear span: distance between the center of the load and the center of the support in the span direction | h | slab or beam thickness |
| a_c, a_t | dimensionless coefficients in damage model from Alfarah et al. [39] | η | coefficient used in the stress-strain behavior model from EN 1992-1-1:2004 ($\eta = \epsilon_c / \epsilon_{c1}$) |
| a_v | clear shear span: clear distance between the face of the load and the face of the support in the span direction | k | plasticity number from stress-strain behavior model in EN 1992-1-1:2004 ($k = E_{ci} / E_{c1}$) |
| b_c | dimensionless coefficients from damage evolution models in compression (assumed = 0.7 based in the model from Birtel and Mark [37], in Krätzig and Pölling [22] and calculated with specific expression in Alfarah et al. [39]) | K_c | factor that controls the shape of the yielding surface (CDP) |
| b_{load} | size of the load in the span direction | l_{c1}, l_{c2} | slab overhang length in supports 1 and 2, respectively |
| b_{slab} | beam or slab width | l_{eq} | characteristics length related to the element size in the mesh |
| b_t | dimensionless coefficients from damage evolution models in tension ($b_t = 0.1$ in Birtel and Mark [37] and calculated with specific expression in Alfarah et al. [39]) | l_{load} | size of the load in the transverse direction |
| $c_1; c_2$ | constants in the tension behavior model from Hordijk [31] | l_{span} | span length between supports |
| d | damage parameter | l_{total} | slab total length in the span direction |
| d_c | damage parameter in compression | V_{Fu} | maximum shear force applied in the test caused by the concentrated load F_u |
| d_g | maximum aggregate size of concrete | w | crack opening |
| d_l | effective depth of the longitudinal reinforcement | w_1 | crack opening corresponding to $f_{ct}/3$ in [29], $w_1 = 0.8G_f/f_{ct}$ |
| d_t | damage parameter in tension | w_2 | critical crack opening or fracture crack opening in [29], $\sigma_t (w_2) = 0$. |
| e | flow potential eccentricity (CDP) | w_c | critical crack opening or fracture crack opening in [31], $\sigma_t (w_c) = 0$. |
| E_0 | undamaged modulus of elasticity of concrete | α_i | coefficient to determine the reduced concrete elastic modulus ($E_c = \alpha_i \bullet E_{ci}$) |
| E_c | modulus of elasticity of concrete | α_t | coefficient that controls the shape of the tensile stress-strain behavior model in Guo [21] |
| $E_{c,sec}$ | secant modulus of elasticity of concrete for $\sigma_c = 0.4f_{cm}$ | β_{CC} | parameter that controls the shape of the stress-strain graph in Carreira and Chu models [20,33] |
| E_{c1} | secant modulus from the origin to the peak compressive stress | γ_c | factor the controls the shape of the stress-strain behavior model after the peak compressive strength in Krätzig and Pölling [22] |
| E_{ci} | tangent modulus of deformation of concrete for zero stress | ϵ_{0c}^{el} | elastic compressive strain |
| E_{cm} | measured modulus of elasticity of concrete | ϵ_c | total compressive strain ($\epsilon_c = \epsilon_c^{pl} + \epsilon_{0c}^{el}$) |
| E_s | steel modulus of elasticity | ϵ_{c1} | compressive strain corresponding to the maximum compressive stress f_{cm} |
| F | applied concentrated load | ϵ_c^{in} | inelastic compressive strain |
| F_{EXP} | maximum concentrated load applied in the test (failure load) | ϵ_c^{pl} | plastic compressive strain |
| F_{FEM} | maximum concentrated load applied in the finite element model (failure load) | ϵ_t | total tensile strength ($\epsilon_t = \epsilon_t^{pl} + \epsilon_t^{el}$) |
| F_u | maximum concentrated load applied in the test (failure load) | $\epsilon_{t,cr}$ | tensile strain at peak tensile stress |
| G_{ch} | Crushing energy | ϵ_t^{el} | elastic tensile strain |
| G_f | Tensile fracture energy | ϵ_t^{in} | inelastic tensile strain |
| G_{f0} | coefficient related to maximum aggregate size | ϵ_t^{pl} | tensile plastic strain |
| $f_{c,cube}$ | concrete compressive strength measured on cube specimens | μ | viscosity parameter (CDP) |
| f_{c0} | limit stress of linear compressive branch | ρ_l | flexural reinforcement ratios in the longitudinal direction (span direction) |
| f_{ck} | characteristic compressive strength of concrete | ρ_t | flexural reinforcement ratios in the transverse direction |
| f_{cm} | mean compressive strength of concrete (measured in cylinders) | σ_{b0}/σ_{c0} | ratio of initial equibiaxial compressive yield stress to initial uniaxial compressive yield stress (CDP model) |
| f_{ct} | concrete tensile strength (peak value) | σ_c | compressive stress |
| f_{ct0} | limit stress of linear tensile branch | σ_t | tensile stress |
| f_{ctm} | measured concrete tensile strength | ψ | Dilation angle for the concrete damaged plasticity model (CDP) |
| | | δ | slab deflection below the load |

(3D) non-linear finite element analyses (NLFEA). However, the following gaps were identified:

- (i) A limited number of studies addressed the challenge of using the same modeling strategy to assess the ultimate capacity of RC members that may develop different shear failure mechanisms (one-way shear and punching shear), such as one-way slabs under concentrated loads [15,16]. Therefore, it is not clear if a calibrated modeling approach to deal with one-way shear, for instance, would also lead to accurate predictions of punching shear capacity.

- (ii) The methodology used in several recent publications with numerical studies also needs to be discussed. For instance, during the validation step of the numerical models, it is frequent to use only one test result with a specific failure mechanism for validating the modeling strategy [17]. However, other failure mechanisms could appear when performing parametric analyses with significant changes in material and geometry parameters. In this way, such different failure mechanisms should also be investigated during the validation step to ensure that the modeling strategy would also represent these accurately.

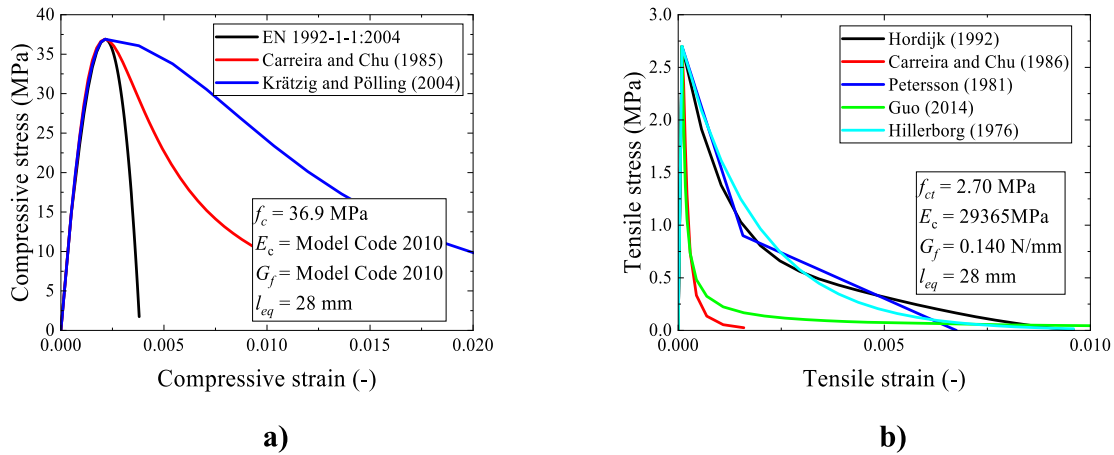


Fig. 1. Comparison of different stress–strain models to describe the behavior under a) compression and b) tension for normal strength concretes.

(iii) Some modeling options are frequently not discussed in numerical studies. For instance, the influence of considering or not the concrete damage evolution parameters (degradation of the elastic modulus) was scarcely investigated [13]. Until now, most studies that propose not using the damage evolution law for simulating static tests assume that this material characteristic would influence only cyclic tests. However, some papers have already shown that this parameter may have a not insignificant influence on the numerical results [13]. Herein, it is assumed that the variation of the elastic stiffness from concrete could influence the confining conditions on three-dimensional problems. Additionally, some mechanical models of one-way shear strength already include the elastic modulus from concrete as a critical parameter in the predictions of ultimate capacity [18]. Since no specific study was found on this matter, the results of NLFEA with and without the damage evolution parameters should be investigated.

This study investigates the accuracy of a developed modeling strategy to represent different shear failure mechanisms that can take place for one-way slabs under concentrated loads: one-way shear as wide beams and punching shear. Besides that, a sensitivity study is performed to show the influence of some modeling choices from the constitutive model adopted in the numerical results. The following parameters are investigated: (i) the influence of considering or not the concrete damage evolution (variation of the elastic modulus in the concrete non-linear phase); (ii) the influence of the stress–strain behavior adopted in compression and tension; and (iii) the viscosity parameter.

Firstly, some important modeling options regarding concrete modeling are discussed in Section 2. Next, the selected tests from Reifßen, Classen and Hegger [8] used as references are detailed in Section 3. In the following (Section 4), the modeling strategy proposed is presented, detailing the constitutive models, material models, and finite element types used. In the validation step (Section 5), the numerical results are compared to the experimental results in terms of failure mechanism and ultimate load. The sensitivity study section (Chapter 6) presents the results of changing specific material parameters of the numerical models.

As a limitation of the study, the presented analysis focuses on the Ultimate Limit States (ULS) without including the effect of delayed shrinkage and creep as well as the possible reduction of tension stiffening at the slabs due to the age of the test (Serviceability Limit States - SLS). The precise estimation of the effect of creep and shrinkage on the SLS of flat slabs and slab-columns connections can be consulted elsewhere [19].

Table 1

Expressions to determine the stress–strain behavior in compression.

| Reference | Expressions |
|--|--|
| EN 1992-1-1:2004 [28] and fib Model Code 2010 [27] | $\sigma_c(\epsilon_c) = f_{cm} \frac{k \cdot \eta - \eta^2}{1 + (k - 2) \cdot \eta} \quad (4)$ $k = 1.05 \cdot E_c \cdot \frac{\epsilon_{c1}}{f_{cm}} \quad (5)$ $\eta = \frac{\epsilon_c}{\epsilon_{c1}} \quad (6)$ |
| Carreira and Chu [20] | $\frac{\sigma_c(\epsilon_c)}{f_{cm}} = \frac{\beta_{CC} \cdot (\epsilon_c / \epsilon_{c1})}{\beta_{CC} - 1 + (\epsilon_c / \epsilon_{c1})^\beta} \quad (7)$ $\beta_{CC} = \frac{1}{1 - \frac{f_{cm}}{\epsilon_{c1} \cdot E_c}} \quad (8)$ |
| Krätzig and Pölling [22] | $\sigma_c(\epsilon_c) = E_c \cdot \epsilon_c, \text{ with } 0 \leq \sigma_c \leq 0.4 \cdot f_{cm} \quad (9)$ $\sigma_{c,2}(\epsilon_c) = \frac{E_{ci} \cdot \frac{\epsilon_c}{f_{cm}} - (\frac{\epsilon_c}{f_{cm}})}{1 + (E_{ci} \cdot \frac{\epsilon_c}{f_{cm}} - 2) \cdot \frac{\epsilon_c}{\epsilon_{c1}}} \cdot f_{cm}, \text{ with } 0.4 \cdot f_{cm} \leq \sigma_c \leq f_{cm} \quad (10)$ |
| | $\sigma_{c,3}(\epsilon_c) = (\frac{2 + \gamma_c \cdot f_{cm} \cdot \epsilon_{c1}}{2 \cdot f_{cm}} \cdot \epsilon_c - \gamma_c \cdot \epsilon_c + \frac{\epsilon_c^2 \cdot \gamma_c}{2 \cdot \epsilon_{c1}}), \text{ with } \epsilon_c > \epsilon_{c1} \quad (11)$ <p>With:</p> $\gamma_c = \frac{\pi^2 \cdot f_{cm} \cdot \epsilon_{c1}}{2 \cdot [\frac{G_{ch}}{l_{eq}} - 0.5 \cdot f_{cm} \cdot (\epsilon_{c1} \cdot (1 - b_c) + b_c \cdot \frac{f_{cm}}{E_c})]^2} \quad (12)$ $b_c = \frac{\epsilon_c^{pl}}{\epsilon_c^{in}}; G_{ch} = (\frac{f_{cm}}{f_{ct}})^2 \cdot G_f \quad (13)$ |

2. Modeling options

2.1. Stress–strain behavior in compression

Several models were proposed in the literature to describe the non-linear behavior of normal-strength concrete in compression [20–24], which differ mainly in the post-peak behavior (Fig. 1a). This occurs because some models include parameters related to the finite element size l_{eq} and crushing energy G_{ch} to soften the degradation of stresses under compression [22,24]. In Fig. 1a, the model of Krätzig and Pölling [22] considers the crushing energy G_{ch} , which was calculated through the following expression [25], which is dependent on the tensile fracture energy G_f :

$$G_{ch} = \left(\frac{f_{cm}}{f_{ct}}\right)^2 \cdot G_f \quad (1)$$

In the absence of experimental data, the fracture energy G_f is generally determined according to fib Model Code 1990 [26] or fib Model Code 2010 expressions [27]. According to fib Model Code 1990 [26], the fracture energy can be calculated as:

Table 2
Expressions to determine the stress–strain behavior in tensile.

| Reference | Expressions |
|------------------------|--|
| Hordijk [31] | $\frac{\sigma_t(w)}{f_{ct}} = [1 + (c_1 \frac{w}{w_c})^3] \cdot e^{-c_2 \frac{w}{w_c}} - \frac{w}{w_c} \cdot (1 + c^3) \cdot e^{-c_2}$ (15) With: $c_1 = 3$; $c_2 = 6.93$; w_c is the critical crack opening or fracture crack opening: $w_c = 5.14 \cdot \frac{G_f}{f_{ct}} \quad (16)$ |
| Petersson [29] | $\sigma_t(w) = f_{ct} \frac{(f_{ct} - \frac{1}{3}f_{ct})}{w_1} \cdot w, \text{ if } w \leq w_1 \quad (17)$ $\sigma_t(w) = \frac{w_1 \cdot \frac{1}{3}f_{ct}}{w_2 - w_1} - \frac{1}{3}f_{ct} \cdot w, \text{ if } w_1 \leq w \leq w_2 \quad (18)$ |
| Hillerborg et al. [32] | $\sigma_t(w) = f_{ct} \cdot e^{-\frac{w}{G_f}} \quad (19)$ |
| Carreira and Chu [33] | $\sigma_t(\varepsilon_t) = f_{ct} \cdot \frac{\beta_{CC}(\varepsilon_t/\varepsilon_{t,cr})}{\beta_{CC} - 1 + (\varepsilon_t/\varepsilon_{t,cr})^\beta} \quad (20)$ $\beta_{CC} = (\frac{f_{cm}}{32.4})^3 + 1.55 \quad (21)$ |
| Guo [21] | $\frac{\sigma_t(\varepsilon_t)}{f_{ct}} = \begin{cases} 1.2 \cdot (\varepsilon_t/\varepsilon_{t,cr}) - 0.2 \cdot (\varepsilon_t/\varepsilon_{t,cr})^6, & \text{if } \varepsilon_t/\varepsilon_{t,cr} \leq 1 \\ \frac{\varepsilon_t/\varepsilon_{t,cr}}{\alpha_t \cdot [(\varepsilon_t/\varepsilon_{t,cr}) - 1]^{1.7} + \varepsilon_t/\varepsilon_{t,cr}}, & \text{if } \varepsilon_t/\varepsilon_{t,cr} > 1 \end{cases} \quad (22)$ $\alpha_t = 0.312 \cdot f_{ct}^{(23)}$ |

$$G_f = \begin{cases} G_{f0} \cdot \left(\frac{f_{cm}}{10}\right)^{0.7}, & \text{if } f_{cm} \leq 80 \text{MPa} \\ 4.3 \cdot G_{f0}, & \text{if } f_{cm} > 80 \text{MPa} \end{cases} \quad (2)$$

with $G_{f0} = 0.025$ N/mm for $d_g = 8$ mm, $G_{f0} = 0.30$ N/mm for $d_g = 16$ mm and $G_{f0} = 0.058$ N/mm for $d_g = 32$ mm. d_g is the maximum aggregate size of concrete. According to the fib Model Code 2010 [27], the fracture energy G_f can be estimated by:

$$G_f = 73 \cdot f_{cm}^{0.18} \quad (3)$$

Table 1 shows the expressions used to determine the stress–strain behavior in compression according to different references (plotted in Fig. 1a).

2.2. Stress–strain behavior in tension

In tension, most models used to describe the non-linear behavior of the concrete provide similar results regarding the relation tensile stress–crack opening displacement [27,29–31]. In Fig. 1b, the models from Hordijk [31], Petersson [29], and Hillerborg et al. [32] account for the fracture energy G_f to describe the softening behavior of concrete in terms of tensile stress \times crack opening ($\sigma_t \times w$). In Fig. 1b, the crack opening w is translated to tensile strains ε_t by the expression:

$$\varepsilon_t = \frac{f_{ct}}{E_c} + \frac{w}{l_{eq}} = \varepsilon_{t,cr} + \varepsilon_t^{in} \quad (14)$$

where $\varepsilon_{t,cr}$ is the undamaged tensile elastic strain and ε_t^{in} is the damaged tensile cracking strain (also named inelastic tensile strain). It can be seen that the expressions from Peterson [29], Hillerborg et al. [32] and Hordijk [31] provide quite similar results (Fig. 1b). Conversely, the curves using the expressions from Carreira and Chu [33] and Guo [21] do not consider the finite element size l_{eq} in the expression and provide quite different post-peak tensile strengths.

Table 2 shows the expressions used to determine the strain–strain behavior in tension according to different references (related to Fig. 1b).

2.3. Damage evolution laws

This study considers the Concrete Damaged Plasticity (CDP) model offered in ABAQUS software to perform the numerical analyses. The effective elastic modulus E varies as a function of the damage parameter

d through the following expression:

$$E = E_0 \cdot (1 - d) \quad (24)$$

where E is the effective elastic modulus and E_0 is the initial or undamaged elastic modulus. d is the damage variable that varies between 0 (undamaged) and 1 (fully damaged). Added to that, the damage parameter also changes the proportion between the inelastic strains and the plastic strains through the following expression:

$$\varepsilon_c^{pl} = \varepsilon_c - \varepsilon_c^{el} = \varepsilon_c^{in} - \frac{d_c}{1 - d_c} \cdot \frac{\sigma_c}{E_0} \quad (25)$$

$$\varepsilon_t^{pl} = \varepsilon_t - \varepsilon_t^{el} = \varepsilon_t^{in} - \frac{d_t}{1 - d_t} \cdot \frac{\sigma_t}{E_0} \quad (26)$$

ε_c^{pl} and ε_t^{pl} are the compressive and tensile plastic strains, respectively; ε_c and ε_t are the total compressive and tensile strains, respectively; ε_{0c}^{el} and ε_t^{el} are the undamaged compressive and tensile elastic strains, respectively; ε_c^{in} and ε_t^{in} are the damaged inelastic strain in compression and damaged tensile cracking strain (or inelastic strain in tension), respectively. From expressions (25) and (26) it can be noted that when the damage parameter is neglected ($d = 0$), the plastic strains become equal to the damaged inelastic strain ($\varepsilon_c^{pl} = \varepsilon_c^{in}$ and $\varepsilon_t^{pl} = \varepsilon_t^{in}$). Therefore, even in simulations of static problems (not cyclic tests), neglecting the damage parameters may influence the simulation results due to its influence on the evolution of plastic strains (or the proportion between plastic and inelastic strains), which deserves more investigation.

Another important aspect of the CDP is how it calculates the uniaxial compressive and tensile strengths (or used stress–strain behavior in compression and tension). In practice, the uniaxial compressive and tensile strengths for a given strain are calculated as follows:

$$\sigma_c = E \cdot (\varepsilon_c - \varepsilon_c^{pl}) = (1 - d_c) \cdot E_0 \cdot (\varepsilon_c - \varepsilon_c^{pl}) \quad (27)$$

$$\sigma_t = E \cdot (\varepsilon_t - \varepsilon_t^{pl}) = (1 - d_t) \cdot E_0 \cdot (\varepsilon_t - \varepsilon_t^{pl}) \quad (28)$$

It shall be noted that considering the damage parameters d_c and d_t changes not only the effective elastic modulus E , but also the plastic strains ε_c^{pl} and ε_t^{pl} . Consequently, for any stress–strain behavior used in the CDP, the damage evolution law will not influence the uniaxial stress–strain behavior considered in the simulations ($\sigma_c \times \varepsilon_c$ or $\sigma_t \times \varepsilon_t$). As a general conclusion, different damage evolution laws will influence exclusively the proportion between plastic ε_c^{pl} and inelastic strains ε_c^{in} in the uniaxial space.

Nevertheless, the CDP uses effective tensile and compressive stress, $\bar{\sigma}_t$ and $\bar{\sigma}_c$, within the yield criterion in the three-dimensional space [34,35], based on the following expressions:

$$\bar{\sigma}_t = \frac{\sigma_t}{(1 - d_t)} = E_0 \cdot (\varepsilon_t - \varepsilon_t^{pl}) = E_0 \cdot \varepsilon_t^{el} \quad (29)$$

$$\bar{\sigma}_c = \frac{\sigma_c}{(1 - d_c)} = E_0 \cdot (\varepsilon_c - \varepsilon_c^{pl}) = E_0 \cdot \varepsilon_{0c}^{el} \quad (30)$$

With the yield criterion defined by the following expression:

$$\frac{1}{1 - \alpha} \left(\sqrt{3} I_2 + \alpha I_1 + \beta (\bar{\sigma}_{max}) - \gamma (\bar{\sigma}_{max}) \right) = c \quad (31)$$

With

$$I_1 = \sigma_1 + \sigma_2 + \sigma_3 \quad (32)$$

$$J_2 = - (1/6) [(\sigma_1 - \sigma_2)^2 + (\sigma_2 - \sigma_3)^2 + (\sigma_3 - \sigma_1)^2] \quad (33)$$

where α , β and γ are material parameters; $\bar{\sigma}_{max}$ is the maximum principal effective stress; $\langle \cdot \rangle$ is the Macauley bracketed; and c is the compression cohesion, with more explanations on these terms given elsewhere [36]. Summing up, the including or not of the damage parameter does not directly influence directly the development of uniaxial stresses but

Table 3
Models of damage evolution law in compression and tensile from literature.

| Reference | Compression | Tension |
|----------------------|---|--|
| Birtel and Mark [37] | $d_c(\varepsilon_c^{in}) = 1 - \frac{\sigma_c/E_0}{\varepsilon_c^{in} \cdot (1 - b_c) + \sigma_c/E_0}$ With $b_c = 0.7$ [37,40] | $d_t(\varepsilon_t^{in}) = 1 - \frac{\sigma_t/E_0}{\varepsilon_t^{in}(1 - b_t) + \sigma_t/E_0}$ With $b_t = 0.1$ [37,40] |
| Yu et al. [41] | $0, \text{ if } \varepsilon_c < \varepsilon_{c1}$ $d_c(\varepsilon_c) = \left\{ \begin{array}{l} 1 - \frac{\sigma_c}{f_{cm}}, \text{ if } \varepsilon_c > \varepsilon_{c1} \end{array} \right.$ | $0, \text{ if } \varepsilon_t < \varepsilon_{tcr}$ $d_t(\varepsilon_t) = \left\{ \begin{array}{l} 1 - \frac{\sigma_t}{f_t}, \text{ if } \varepsilon_t > \varepsilon_{tcr} \end{array} \right.$ |
| Alfarah et al. [39] | $d_c(\varepsilon_c^{in}) = 1 - \frac{1}{2 + a_c} \left[\frac{2(1 + a_c) \exp(-b_c \varepsilon_c^{in})}{-a_c \exp(-2b_c \varepsilon_c^{in})} \right] a_c = 2 \cdot \frac{f_{cm}}{f_{c0}} - 1 + 2 \cdot \sqrt{\left(\frac{f_{cm}}{f_{c0}}\right)^2 - \frac{f_{cm}}{f_{c0}}} =$ $7.873b_c = \frac{f_{c0} \cdot l_{eq}}{G_{ch}} \left(1 + \frac{a_c}{2}\right)$ With $f_{c0} = 0.4f_{cm}$ | $d_t(\varepsilon_t^{in}) = 1 - \frac{1}{2 + a_t} \left[\frac{2(1 + a_t) \exp(-b_t \varepsilon_t^{in})}{-a_t \exp(-2b_t \varepsilon_t^{in})} \right] a_t = 2 \cdot \left(\frac{f_{ct}}{f_{ct0}}\right) - 1 + 2 \cdot \sqrt{\left(\frac{f_{ct}}{f_{ct0}}\right)^2 - \frac{f_{ct}}{f_{ct0}}} = 1$ $b_t = \frac{f_{ct0} \cdot l_{eq}}{G_f} \left(1 + \frac{a_t}{2}\right)$ With $f_{ct0} = f_{ct}$ |

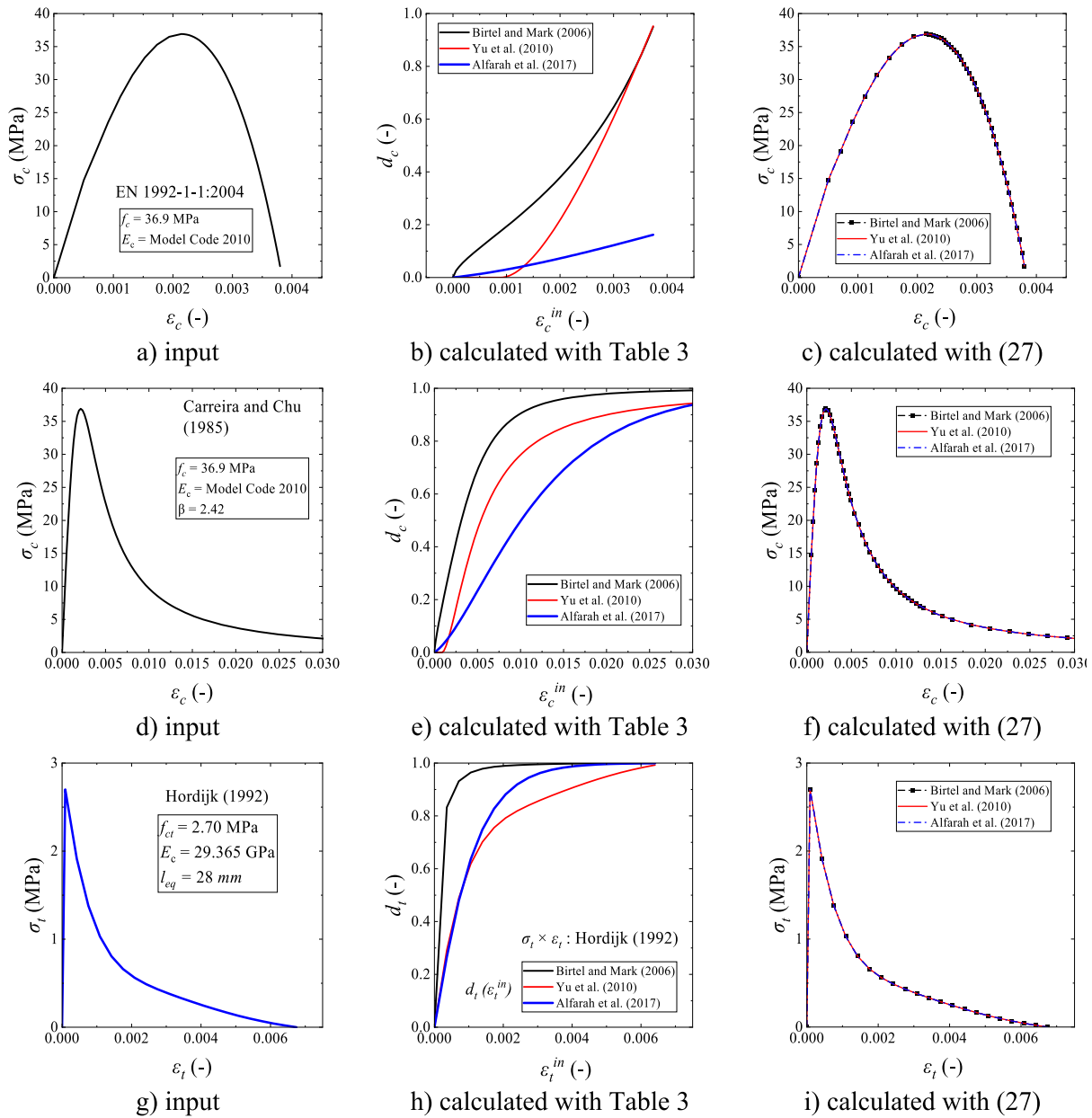


Fig. 2. Damage evolution: a) stress–strain behavior in compression according to [28]; b) damage evolution graphs (Table 3); c) calculated stress–strain behavior with Eq. (27), using calculated values of damage and plastic strains. d) stress–strain behavior in compression according to [20]; e) damage evolution graphs (Table 3); f) calculated stress–strain behavior with Eq. (27); g) stress–strain behavior in tensile according to [31]; h) damage evolution graphs from Table 3; i) calculated stress–strain behavior with Eq. (27). e.

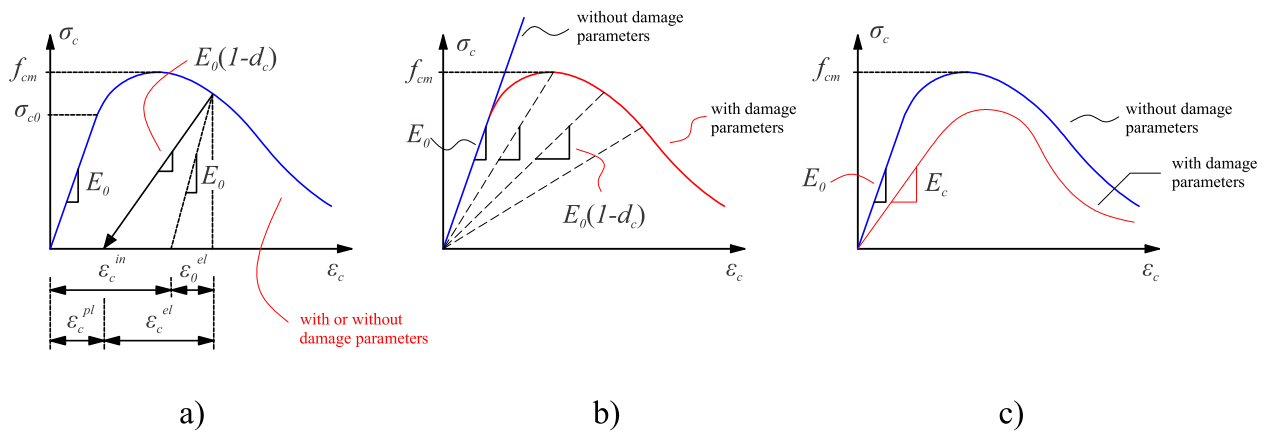


Fig. 3. A) stress–strain behavior in compression considered in the Concrete Damaged Plasticity (CDP); b) stress–strain behavior model with and without damage parameters considered by pure damage models; c) erroneous assumption of stress–strain behavior when considering damage parameters.

influences the triaxial stresses evolution.

Table 3 presents three different damage evolution laws. The model from Birtel and Mark [37] determines the damage parameters d_c and d_t only based on the inelastic strains ϵ_c^{in} and ϵ_t^{in} . Consequently, the model from Birtel and Mark [37] considers that damage occurs even before reaching the peak compressive strength f_{cm} . The model presented by Yu et al. [38] is a simpler way to estimate the damage evolution parameters since it depends only on the stress values σ_c and σ_t after the critical compressive strain ϵ_{c1} and critical tensile strain $\epsilon_{c,cr}$ (strain at which the crack starts to open). Therefore, this model assumes that damage occurs only in the post-peak branch of the stress–strain behavior (after reaching f_{cm} or f_{ct}). Consequently, this model assumes that damage does not start exactly when the inelastic strains are larger than zero. The model from Alfarah et al. [39] is similar to the one from Birtel and Mark [37] as it is based on the evolution of inelastic strains. However, the damage model from Alfarah et al. [39] also includes the finite element size l_{eq} in the expressions for compression and tension.

Fig. 2 shows how these damage models differ according to the assumed stress–strain behavior in compression and tension ($\sigma_c \times \epsilon_c$ or $\sigma_t \times \epsilon_t$ entered as input parameters) and the respective stress–strain

behavior effectively used by the CDP model after calculating the damage parameters (Eq. (27) and (28)).

Assuming the stress–strain behavior in compression given by EN 1992-1-1:2004 [28] expressions (Fig. 2a), it can be seen that the results of the damage evolution parameters show significant variability. The model from Birtel and Mark [37] presents a sharper increase in the damage parameters according to the inelastic strains. The model from Alfarah et al. [39] did not reach a value of d_c greater than 0.2 at the peak compressive strain (which seems inconsistent). This occurs because the model from Alfarah et al. [39] was devised to deal with stress–strain models with large residual compressive strength, such as the ones from Carreira and Chu [20] and Krätzig and Pölling [22]. The model from Yu et al. [38] presented an intermediate response between the other models. Using the stress–strain behavior in compression according to the model from Carreira and Chu [20] (Fig. 2d), the differences between the different damage models become less accentuated (Fig. 2e). However, the model from Birtel and Mark [37] still results in a sharp increase in the damage parameters. The damage parameter with the model from Alfarah et al. [39] presents a smoother increase with the inelastic strains but reaches larger values (consistent ones) at the ultimate compressive

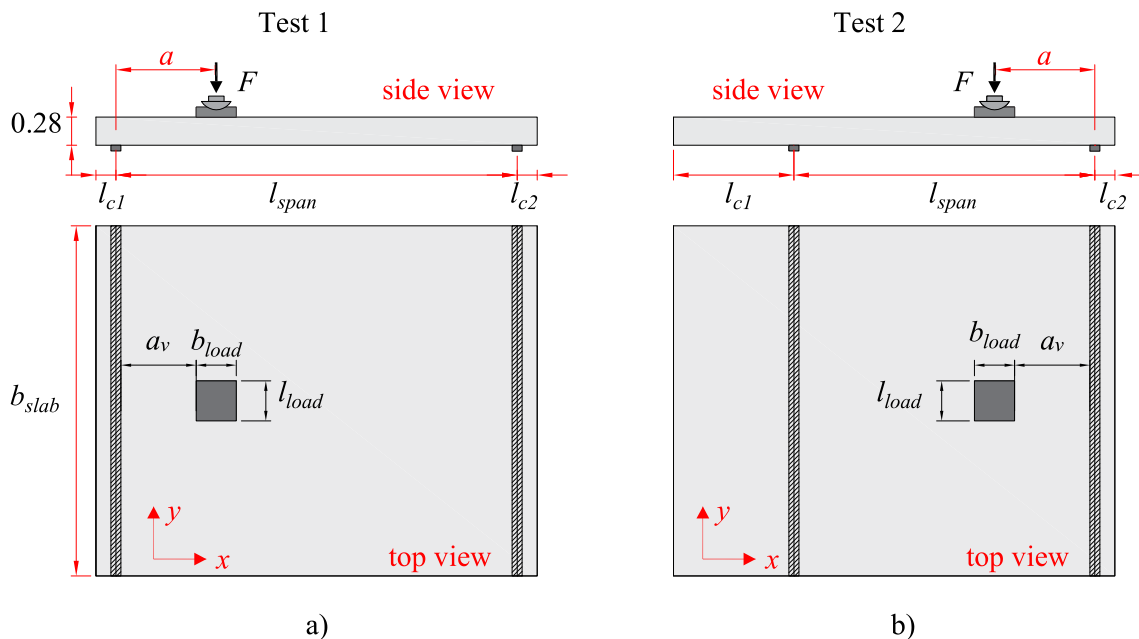


Fig. 4. Schematic view of the geometry of the one-way slabs tested by Reißer, Classen and Hegger (2018) evaluated in this study: a) layout of the first test on the specimens and; b) layout of the second test on the specimens. Source: Adapted from Reißer, Classen and Hegger [8].

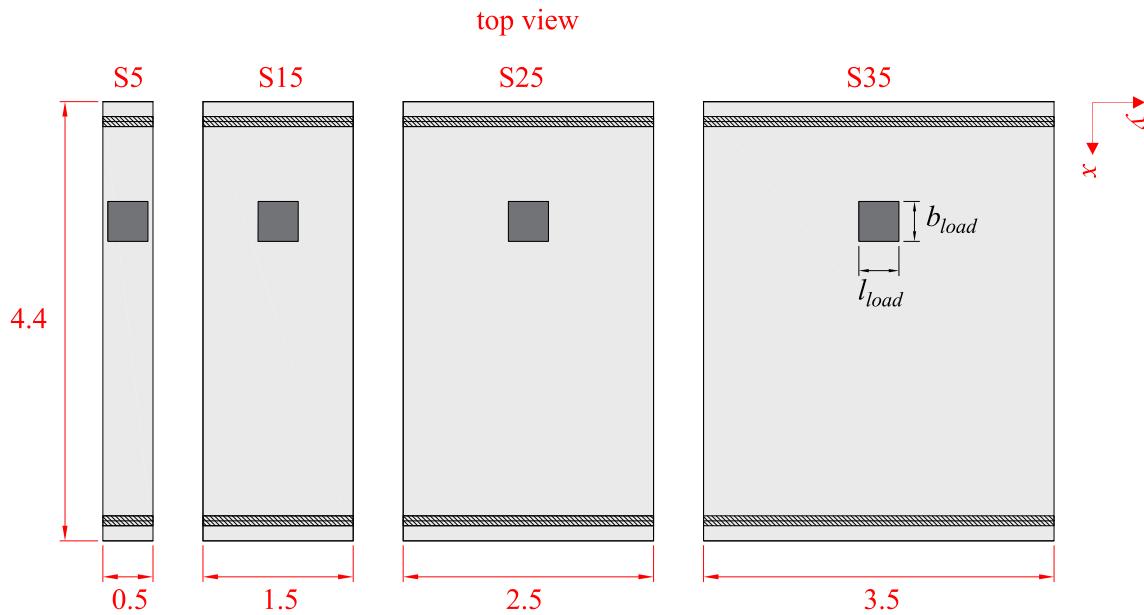


Fig. 5. Layout of some of the tested slabs with varied slab widths. Dimensions in m.

strains. The model from Yu et al. [38] presents intermediate values between the previous ones.

Similar observations can be made for the different damage evolution models in tension (Fig. 2g,h). Besides that, it is shown in Fig. 2c,f,i, that regardless of the different damage models, the equivalent stress-strain behavior used in the CDP is equal to that inserted as input (applying expressions (27) and (28), confirming the previous statement based on the expressions.

It is important to note that the stress-strain behavior with and without the damage parameters will always follow the same envelope (Fig. 3a). Different from pure damage models (Fig. 3b), the post-peak behavior is not influenced by the absence of damage parameters in the CDP. Besides, it is important to observe that the decrease of the effective elastic modulus when including the damage parameters does not result in changes in the uniaxial stress-strain behavior, as could be suggested in Fig. 3c (which represents an erroneous interpretation of the effect of including the damage parameters).

3. Control specimens from literature

3.1. Selection of control specimens

This study uses one-way slabs under concentrated loads tested by Reißer et al. [8] as reference tests. In this set of tests, different failure

mechanisms occurred, varying specifically parameters in the analyses, such as the load position and slab's width. With these experiments, it is possible to illustrate potential problems by using only one test to validate a defined modeling strategy. In total, 13 of 34 tests were selected to be calibrated based on the key parameters in the reported paper by Reißer, Classen and Hegger [8]. The varied parameters are (i) the shear span a defined between axes of support and loading plate and (ii) the slab width b_{slab} . Different failure mechanisms were observed by varying these two parameters (shear, punching or a mixed mode between them). This study did not address the tests with continuity over the support investigated by [8].

3.2. Geometry of control specimens

Fig. 4 and Fig. 5 show the generic geometry of the one-way slabs (control specimens) tested by Reißer, Classen and Hegger [8]. In this study, only the simply supported slabs were evaluated. The span length l_{span} was also changed in some tests, particularly those on which it was possible to perform two tests on the same slab. However, no relation between the span length and the governing failure mechanism was identified [8].

The concrete cover was 20 mm for all slabs. High-strength steel bars ($f_{yk} \approx 900$ MPa) were used for the longitudinal reinforcement on the tension side of the slabs to ensure shear or punching failures instead of

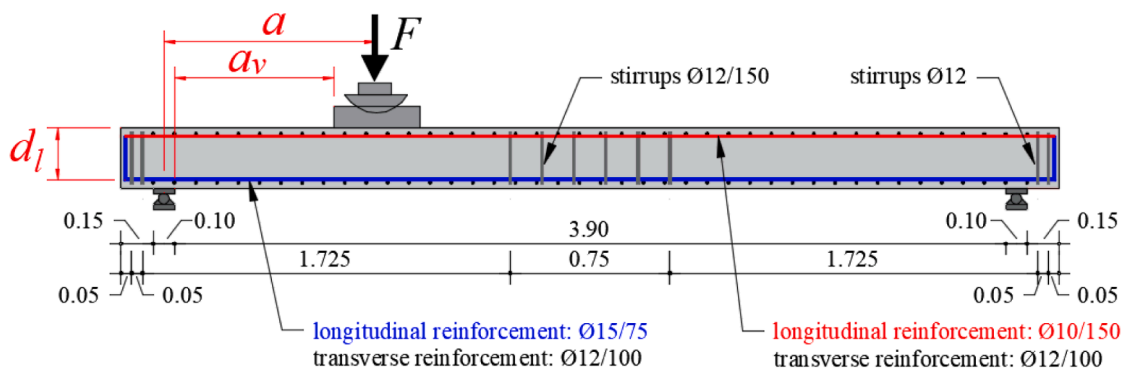


Fig. 6. Reinforcement layout of simply supported slabs with $l_{total} = 4.4$ m tested by Reißer, Classen and Hegger [8]. Dimensions in m.

Table 4
Geometry, test layout and failure load of the control slabs. Source: Reißen, Classen and Hegger (2018).

| Test | l_{c1} (m) | l_{span} (m) | l_{c2} (m) | l_{total} (m) | b_{slab} (m) | h (m) | ρ_l (%) | ρ_t (%) | a/d (-) | a_w/d_t (-) | F_{EXP} (kN) | V_{Fu} (kN) |
|--------|--------------|----------------|--------------|-----------------|----------------|---------|--------------|--------------|-----------|---------------|----------------|---------------|
| S5A | 0.20 | 3.0 | 1.90 | 5.9 | 0.5 | 0.28 | 0.98 | 0.45 | 2.9 | 1.92 | 189 | 145 |
| S5B-1 | 0.20 | 4.0 | 0.2 | 4.4 | 0.5 | 0.28 | 0.98 | 0.45 | 4.2 | 3.17 | 183 | 137 |
| S5B-2 | 1.2 | 3.0 | 0.2 | 4.4 | 0.5 | 0.28 | 0.98 | 0.45 | 4.2 | 3.17 | 215 | 144 |
| S15B-1 | 0.2 | 4.0 | 0.2 | 4.4 | 1.5 | 0.28 | 0.98 | 0.45 | 4.2 | 3.17 | 543 | 407 |
| S15B-2 | 1.2 | 3.0 | 0.2 | 4.4 | 1.5 | 0.28 | 0.98 | 0.45 | 4.2 | 3.17 | 638 | 425 |
| S25B-1 | 0.2 | 4.0 | 0.2 | 4.4 | 2.5 | 0.28 | 0.98 | 0.45 | 4.2 | 3.17 | 664 | 498 |
| S25B-2 | 1.2 | 3.0 | 0.2 | 4.4 | 2.5 | 0.28 | 0.98 | 0.45 | 4.2 | 3.17 | 780 | 520 |
| S35A-1 | 0.2 | 3.0 | 1.2 | 4.4 | 3.5 | 0.28 | 0.98 | 0.45 | 2.9 | 1.92 | 1143 | 876 |
| S35A-2 | 0.2 | 3.0 | 1.2 | 4.4 | 3.5 | 0.28 | 0.98 | 0.45 | 2.9 | 1.92 | 892 | 684 |
| S35B-1 | 0.2 | 4.0 | 0.2 | 4.4 | 3.5 | 0.28 | 0.98 | 0.45 | 4.2 | 3.17 | 985 | 739 |
| S35B-2 | 1.2 | 3.0 | 0.2 | 4.4 | 3.5 | 0.28 | 0.98 | 0.45 | 4.2 | 3.17 | 1024 | 683 |
| S35C-1 | 0.2 | 4.0 | 0.2 | 4.4 | 3.5 | 0.28 | 0.98 | 0.45 | 5.4 | 4.42 | 1066 | 787 |
| S35C-2 | 0.2 | 4.0 | 0.2 | 4.4 | 3.5 | 0.28 | 0.98 | 0.45 | 5.4 | 4.42 | 924 | 623 |

Table 5
Concrete properties described in references. Source: Reißen [15].

| Test | f_{cm} (MPa) | f_{ctm} (MPa) | E_{cm} (MPa) | $f_{ct,pred}$ (MPa) | $\frac{f_{ct,pred}}{f_{cm}} - 1$ (%) | $E_{c,sec,pred}$ (MPa) | $\frac{E_{c,sec,pred}}{E_{cm}} - 1$ (%) |
|--------|----------------|-----------------|----------------|---------------------|--------------------------------------|------------------------|---|
| S5A | 36.9 | 2.7 | 24,200 | 2.83 | 4.6% | 29,365 | 21.3% |
| S5B-1 | 39.2 | 3.0 | 26,200 | 2.97 | -0.9% | 30,140 | 15.0% |
| S5B-2 | 40.5 | 2.8 | 28,100 | 3.06 | 9.1% | 30,571 | 8.8% |
| S15B-1 | 37.7 | 2.8 | 27,300 | 2.88 | 2.8% | 29,637 | 8.6% |
| S15B-2 | 38.2 | 3.0 | 27,600 | 2.91 | -3.0% | 29,805 | 8.0% |
| S25B-1 | 27.9 | 2.5 | 22,400 | 2.20 | -11.9% | 26,133 | 16.7% |
| S25B-2 | 29.5 | 2.6 | 21,000 | 2.32 | -10.8% | 26,735 | 27.3% |
| S35A-1 | 41.3 | 2.7 | 29,900 | 3.11 | 15.0% | 30,834 | 3.1% |
| S35A-2 | 29.0 | 2.7 | 23,300 | 2.28 | -15.4% | 26,549 | 13.9% |
| S35B-1 | 35.9 | 2.8 | 28,200 | 2.76 | -1.4% | 29,023 | 2.9% |
| S35B-2 | 38.2 | 3.0 | *28200 | 2.91 | -3.0% | 29,805 | 5.7% |
| S35C-1 | 39.6 | 2.4 | 27,200 | 3.00 | 24.9% | 30,273 | 11.3% |
| S35C-2 | 29.5 | 2.5 | 22,700 | 2.32 | -7.2% | 26,735 | 17.8% |
| | | | | AVG | 0.2% | AVG | 12.3% |

*assumed value.

flexural failures without increasing the reinforcement ratios. Normal strength steel bars ($f_{yk} = 500$ MPa) were applied in the transverse direction. The longitudinal and transverse reinforcement ratios (ρ_l and ρ_t) on the slab's tension side were fixed at 0.98% and 0.45%, respectively ($\emptyset 15/7.5$ and $\emptyset 12/10$). This resulted in an effective depth of the longitudinal bending reinforcement of $d_l = 0.241$ m and an effective depth of the transverse reinforcement of $d_t = 0.254$ m. The reinforcement layer on the compression side consisted of normal-strength steel bars ($f_{yk} \approx 500$ MPa) with the following distribution: $\emptyset 10/15$ in the longitudinal direction (0.22%) and $\emptyset 12/10$ in the transverse direction (0.45%). Fig. 6 shows the reinforcement layout, including the stirrups ($\emptyset 12$) placed at the support and at the midspan. Reißen, Classen and Hegger [8] used these stirrups to prevent shear failures out of the region studied, to improve the reinforcement anchorage at the supports, and to simplify the installation of the top reinforcement.

Table 4 describes the geometry of the slabs, the layout of the tests (see Fig. 4 and Fig. 5), the reinforcement ratios in the longitudinal and transverse directions, and the failure loads for the 13 investigated tests. The notation of the tests can be illustrated with S25B-1: S means "slab"; the first two numbers following identify the slab width in meter (5: $b_{slab} = 0.5$ m; 15: $b_{slab} = 1.5$ m; 25: $b_{slab} = 2.5$ m; and 35: $b_{slab} = 3.5$ m). The last letter refers to the shear slenderness (A: $a/d_l = 2.9$; B: $a/d_l = 4.2$; C: $a/d_l = 5.4$). The last number means the number of the test (1 = first test; 2 = second test).

3.3. Material properties of control specimens

Table 5 describes the material properties of the concrete used in the tests according to Reißen [15] and Reißen et al. [8]. The main properties used to simulate the concrete behavior are the average tensile strength (f_{ctm}) measured on cores drilled from the slabs ($D \approx 54.5$ mm, $H \approx 110$

mm), the compressive strength measured on cylinder specimens f_{cm} ($D = 150$ mm, $H = 300$ mm), and the mean modulus of elasticity (secant modulus) of concrete E_{cm} (measured at 40% of f_{cm}). Coarse aggregate with a maximum size of 16 mm was used.

To provide some insight into the comparison between tested and predicted material properties, the concrete tensile strength $f_{ct,pred}$ and secant elastic modulus $E_{c,sec,pred}$ were calculated based on the fib Model Code 2010 [27] expressions as (assuming quartzite aggregates):

$$f_{ct,pred} = 0.3 \cdot (f_{ck})^{2/3}, \text{ with } f_{ck} = f_{cm} - 8 \text{ MPa} \quad (34)$$

$$E_{c,sec,pred} = \alpha_i \cdot E_{ci} \quad (35)$$

$$\alpha_i = 0.8 + 0.2 \cdot \frac{f_{cm}}{88} \leq 1 \quad (36)$$

$$E_{ci} = 21500 \cdot \left(\frac{f_{cm}}{10} \right)^{1/3} \quad (37)$$

Table 5 shows that, on average, the predicted tensile strength with the fib Model Code 2010 [27] expressions fit well with the measured values reported by Reißen [15] (the average error was less than 1%, and the maximum deviations were less than 15% except for one outlier). On the other hand, the deviations of $E_{c,pred}$ compared to the measured values were generally larger than 10% and, for the slab S25B-2, reached a maximum of 27.3%. In this study, the measured values of the concrete tensile strength and elastic modulus were adopted in the reference numerical models. Nevertheless, a comparison between the numerical results using measured and predicted values of concrete elastic modulus is also provided in one of the sections (as these values varied more significantly).

The measured yield strength f_y varied between 822 MPa and 920

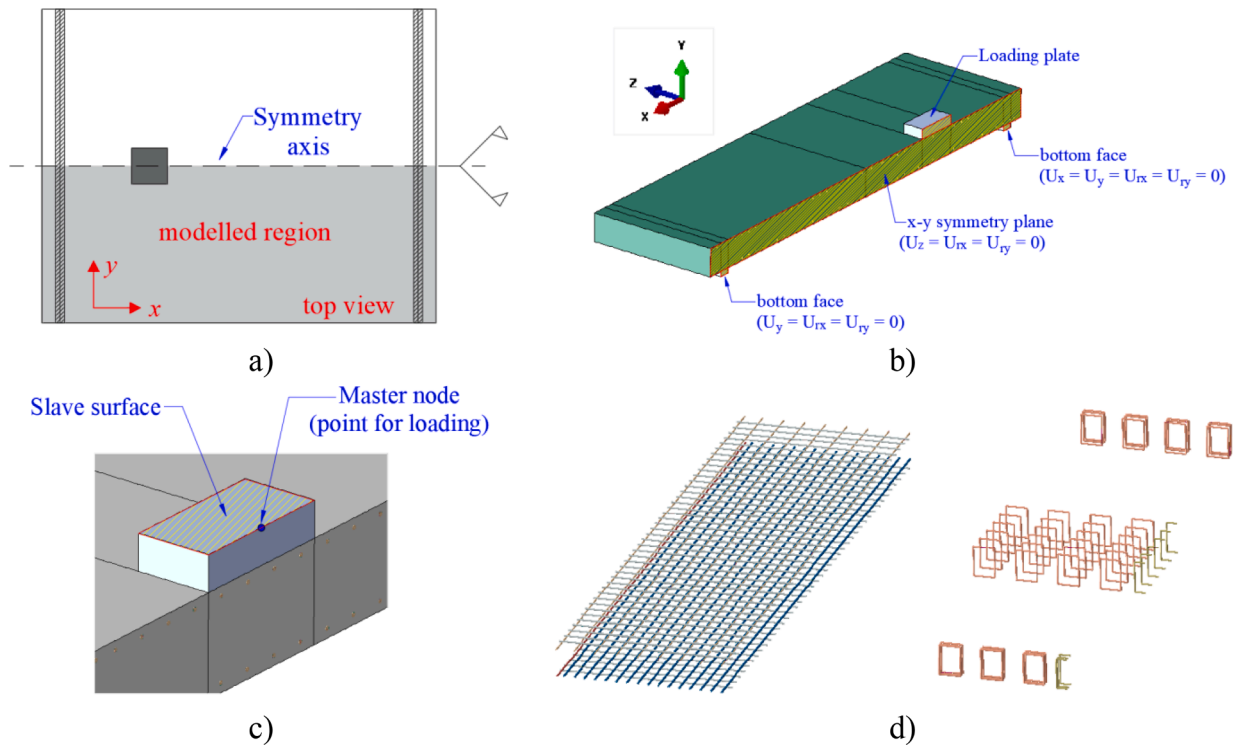


Fig. 7. Boundary conditions in the numerical models: a) detail of the symmetry axis; b) three-dimensional view of the built numerical model; c) detail of the applied load using rigid body displacement with free rotation of the slave surface and d) detail of the longitudinal and transverse reinforcement and stirrups of the modeled slabs.

MPa for the 15 mm diameter bars; 540 MPa to 573 MPa for the 12 mm diameter bars; and it was assumed as 550 MPa for the 10 mm diameter bars. The ultimate tensile strength f_{ult} varied between 1077 MPa and 1110 MPa for the 15 mm diameter bars; 595 MPa to 639 MPa for the 12 mm diameter bars. The average steel elastic modulus E_s was 199 GPa for the 15 mm diameter bars and 200 GPa for the other bars.

4. Finite element simulations

4.1. Overview

The finite element software ABAQUS/CAE [42] was used to model the specimens. By considering the specimens' symmetry, half of the slab's geometry was modeled to reduce the processing time of the numerical models (Fig. 7a). Fig. 7b shows a 3D view of the numerical models with highlighted boundary conditions and symmetry planes. A rigid body interaction was implemented between the center node of the loading plate (master node) and the top surface of the loading plate (slave surface) (Fig. 7c). The rotation of the slab surface was free in relation to the master node. In this way, an axial hinge has been simulated above the loading plate. A similar interaction was also implemented at the supports to allow a free rotation around the Z-axis while the vertical and horizontal displacements were fixed. Fig. 7d shows all reinforcement. The interface between the support plates and loading

plate surface with the slab was modeled assuming (i) hard contact (allowing separation of the surfaces) and (ii) frictionless. A perfect bond between reinforcement and concrete was also assumed based on [14] since no anchorage failure was reported.

4.2. Mesh

Concrete parts, supporting plates and loading plates are meshed with 8-node hexahedral solid elements with reduced integration (C3D8R). Reduced integration was considered to avoid the undesirable shear locking of the brick elements [42,43]. The rebars were modeled with 2-node truss elements (T3D2). Two mesh discretizations were used for the concrete parts to optimize the time of processing (Fig. 8). In the region closer to the loading plate, where failure was expected to occur, the element size for concrete and reinforcement parts was chosen as 28 mm, which allows having 10 elements over the thickness of the model. In the second part of the slab, the element size used was approximately 56 mm. The interaction between the two parts of the slab was performed by a tied contact, which allows different mesh discretization between the two regions.

4.3. Solution procedure

The simulations were conducted using ABAQUS/Standard package

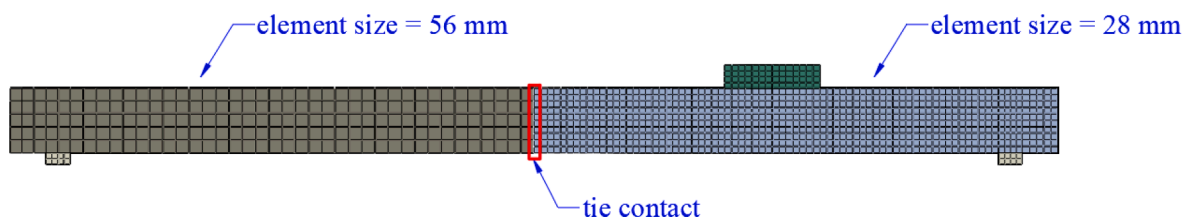


Fig. 8. Sketch of the mesh discretization applied in the numerical models.

[42], on which different implicit solution procedures are available. This study used the Newton-Raphson algorithm in the incremental-iterative procedure. In summary, the Newton-Raphson algorithm divides the analysis process into a series of load increment steps, iterating several times in each incremental step until finding an acceptable solution (based on convergence criteria), and then solving the next incremental step. In the end, the sum of all incremental responses is the approximate solution of the nonlinear analysis [44]. The convergence criteria were based on force (0.5% in the comparison between internal and external forces of the numerical model) and displacement (1% in the comparison between the applied displacement and the measured displacement for each increment). The automatic increment size definition from ABAQUS was used, on which the increment size is reduced to 25% of its original value if the solution seems to diverge, and it increases the increment size by 50% if convergence is achieved smoothly (if less than 4 iterations are needed in two consecutive increments) [45]. The maximum number of iterations allowed in a given increment is 16 (default value), and the maximum number of cutbacks per increment is set as 5. Therefore, if convergence is not achieved for a given increment size, 5 cutbacks and 16 iterations for each increment size are allowed before stopping the simulation.

4.4. Material modeling

The CDP model is grounded on three main parts: (i) damage evolution, yield criterion, and plastic flow rule [42]. The damage evolution laws describe how the elastic stiffness E_0 is degraded with increasing strains. The yield criterion is described according to Lubliner [34] and further modified by Lee and Fenves [35]. The plastic flow in the CDP used the non-associated potential plastic flow hypothesis. CDP uses a potential function G that assumes a Drucker-Prager type hyperbolic form [46]. Further details on the expressions that describe the CDP model can be consulted elsewhere [13].

The required input data for the CDP to represent the concrete compressive behavior are the relations between (i) the compressive stress σ_c with the inelastic compressive strains ϵ_c^m , and (ii) the evolution of the compressive damage variable d_c according to the compressive damage inelastic strains ϵ_c^m . For concrete in tension, the required input are the relations between (i) the tensile stress σ_t with tensile cracking strain ϵ_t^m and (iii) the evolution of the tension damage variable d_t with the tensile cracking strain ϵ_t^m [36]. The auxiliary input parameters to define the yield criterion and the plastic flow rule are the dilation angle ψ ; the shape factor K_c ; the eccentricity parameter e ; the viscosity parameter μ , and the ratio between the biaxial compressive strength σ_{b0} and the uniaxial compressive strength σ_{c0} .

The stress–strain behavior under compression was modeled according to the expressions from the current *fib* Model Code 2010 and EN 1992-1-1:2005 [47] (see Table 1). In these expressions, ϵ_{c1} is the strain at peak stress and it was calculated according to EN 1991-1:2005 [47]:

$$\epsilon_{c1} = \frac{0.7 \cdot f_{cm}^{0.31}}{1000} \quad (38)$$

The tensile stress–strain behavior was modeled using Hordijk's model [31], which considers the bandwidth l_{eq} to reduce the mesh sensitivity of the results through the same approach described by Genikomsou and Polak [13]. In this study, the value of l_{eq} was assumed to be equal to the average finite element size (28 mm and 56 mm, respectively, in the different regions of the slab). The fracture energy G_f was determined according to *fib* Model Code 2010 expressions [27]. The model of Alfarah et al. [39] was chosen to determine the damage evolution in tension since it accounts for the bandwidth length l_{eq} in tension. Therefore, this model can avoid any mesh sensitivity issues due to tension cracking. The damage parameter evolution in compression was determined according to Birtel and Mark [37] to avoid the overly low values of d_c at the ultimate compressive strains when using the model from Alfarah et al. [39] (see Fig. 2b).

Table 6

CDP model parameters used for the reference numerical analyses.

| Parameter | Reference |
|---|-----------------------------|
| Yield criterion | |
| Compressive behavior ($\sigma_c \times \epsilon_c^m$) | EN 1992-1-1:2004 [14,28,31] |
| Tensile behavior ($\sigma_t \times \epsilon_t^m$) | Hordijk [31] |
| Damage evolution | |
| Compression damage ($d_c \times \epsilon_c^m$) | Birtel and Mark [37] |
| Tensile damage ($d_t \times \epsilon_t^m$) | Alfarah et al. [39] |
| Plasticity parameters | |
| Dilation angle, Ψ (°) | 30 |
| σ_{b0}/σ_{c0} | 1.16 [53,54] |
| Parameter K_c | 0.66 [42] |
| Eccentricity, e | 0.1 |
| Viscosity parameter μ | 0.00001 |
| Fracture energy, G_f | <i>fib</i> Model Code 2010 |
| f_{ct} | measured (Table 5) |

4.5. Plasticity parameters

The plasticity parameters were chosen based on the literature review [13,43,48–51]. The dilation angle adopted for the concrete was 30°. Notably, this value is close to that expected by Poliotti and Bairan [52] for the maximum dilation angle of normal strength concretes ($\psi = 32^\circ$) based on inverse analyses of experimental investigations. The fracture energy G_f was calculated according to the *fib* Model Code 2010 [27] since the values with the *fib* Model Code 1990 [26] underestimated the ultimate capacity of the tests that failed by punching. The default value of the ratio σ_{b0}/σ_{c0} in ABAQUS is 1.16 for the concrete. This value is based on the experimental tests of Kupfer et al. [53,54].

The viscosity parameter value chosen was 0.00001 in such a way as to decrease the sensitivity of the results to the viscoplastic regularization in ABAQUS/Standard (implicit integration). However, in the literature, the values applied to vary significantly: between 0.00001 and 0.05, for instance [14,17,55–57]. In practice, a viscosity parameter is a numerical tool used in the CDP model to improve convergence and eventually increase the speed of the simulation through the damping of the crack propagation through the numerical models. In practice, using higher values of the viscosity parameter makes cracks not concentrate in small regions and the damaged region increases considerably [58]. However, for higher viscosity values, such as 0.001, the material may show a perfect plastic behavior (which means that the residual tensile strength, for instance, keeps being the maximum tensile strength during the full simulation after cracking) [58].

4.6. Summary of the material parameters of the reference FEM

Table 6 summarizes the main information about the materials models adopted for concrete in the reference numerical models.

5. Validation of the modelling approach

5.1. Level of accuracy according to the slab width

Fig. 9 compares the finite element model (FEM) results and the experimental results (EXP) in terms of applied load at failure and governing failure mechanism (shape of the graphs). The statistics about the level of accuracy with the proposed approach are discussed in more detail in the next sections (relation between tested and predicted resistances, Section 5.3).

Excluding the results of S5A, which will be described in more detail next, the results of the numerical models approximate fairly well the applied loads at failure from the experiments. Moreover, all numerical results clearly indicate a sharp decrease in the load capacity after failure, which is a well-known characteristic of brittle failure mechanisms such as shear and punching failures. Most predictions with the FEM deviate less than 20% from the test results for the ultimate load F_{EXP} . The only

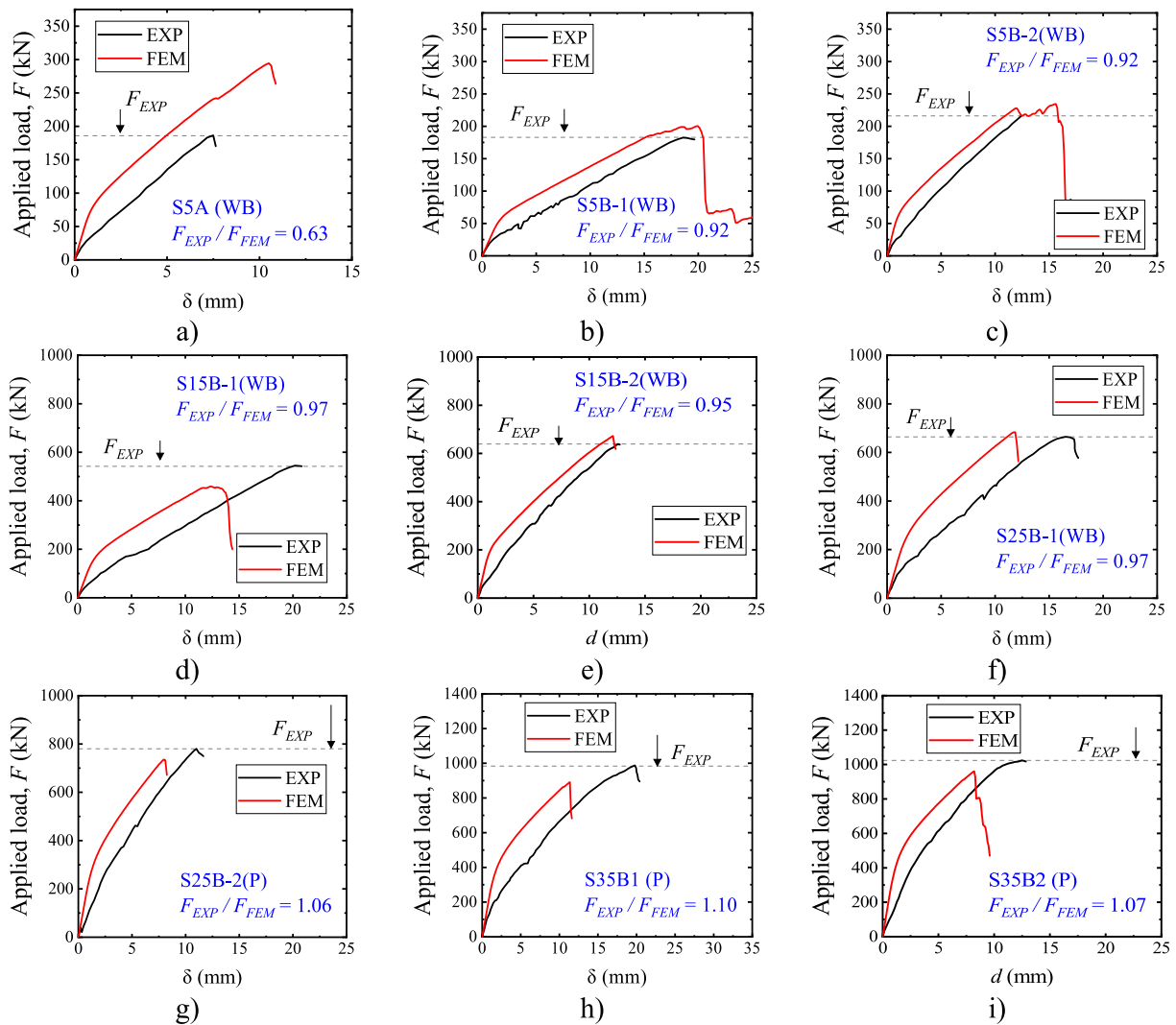


Fig. 9. Comparison between numerical (FEM) and experimental results (EXP) for the tests a) S5A; b) S5B-1; c) S5B-2; d) S15B-1; e) S15B-2; f) S25B-1; g) S25B-2; h) S35B-1; and i) S35B-2.

exception in Fig. 9 was the test S5A, on which the FEM result overestimated the failure load by approximately 38%. Yielding of the reinforcement at failure was observed in none of the numerical models, which also agrees with the test results.

Since the presented modeling approach does not include a specific calibration for each test (for instance, regarding the concrete tensile strength, fracture energy or dilation angle), the level of accuracy is considered satisfactory in a global way. In other words, this study

follows the same modeling strategy for all tests using the same expressions and values of material parameters for all tests. The offset between the numerical and experimental graphs (with a stiffer response in the numerical results) can be attributed to rubber layers placed between the slabs and supports in the experimental program, which was not modeled in this study as simplification.

In this study, the test result from S5A may indicate some limitations of the proposed modeling approach. Since this test corresponds to a

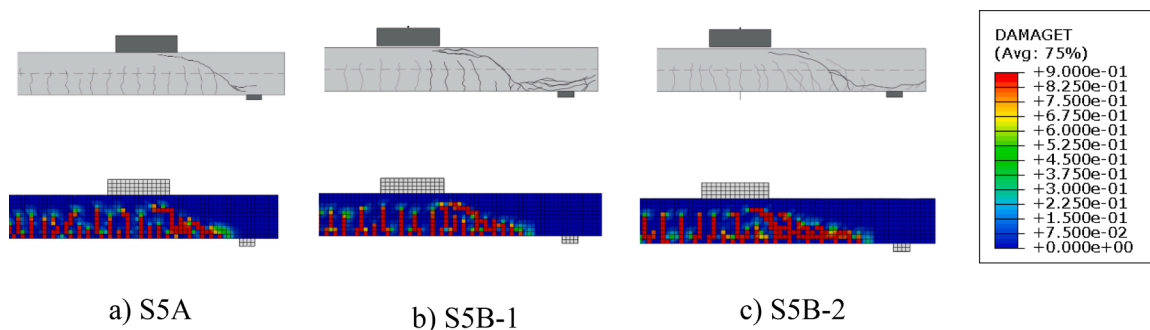


Fig. 10. Comparison between crack patterns after the failure of experimental tests and FE models for a) S5A; b) S5B-1; c) S5B-2. Note: DAMAGET is the damage variable in tension.

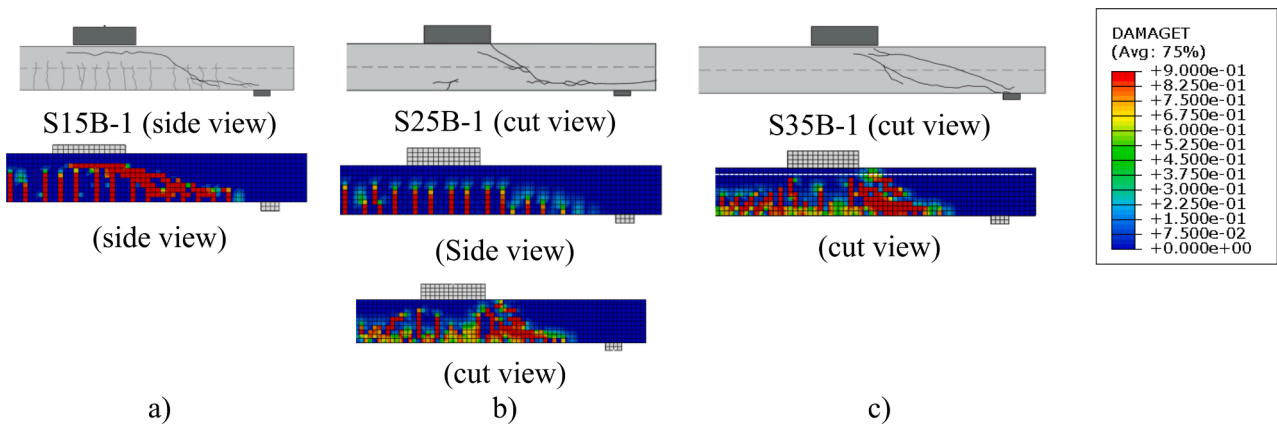


Fig. 11. Comparison between the FE models and the test results in terms of the cracking pattern for: a) S15B-1; b) S25B-1; c) S35B-1. DAMAGET is the scalar damage variable in tension.

lower shear slenderness ($a/d_l = 2.9$ and $a_v/d_l = 1.92$), it may have benefited from arching action in the numerical model in a more straightforward way compared to the test result. In practice, comparing the test results of S5A and S5B-1, the ultimate load F_{EXP} from these tests is approximately the same, regardless of the lower shear slenderness a_v/d_l for the test S5A compared to S5B-1 (1.92 compared to 3.17). This means that the numerical model may have some limitations in representing non-slender beams' one-way shear failure mechanism due to the higher sensibility of such tests with the cracking pattern evolution and the larger scatter in the arching action efficiency. Similar problems, for instance, were found by Henze [16] modeling cantilever slabs when the load was placed close to the support ($a_v/d_l = 1$ and $a_v/d_l = 2$). At the same time, this result could also indicate that the test result S5A did not behave as it would be expected. Proof of that is that other tests were performed by Reißer, Classen and Hegger [8] with lower shear slenderness, and they achieved a significantly higher failure load (tests S5-D, S5D-L8, S5E-L8).

well reproduced by the numerical models, regardless of the governing failure mechanism (the tensile damage variable, DAMAGET, is plotted to represent the cracking pattern). In Fig. 10, the numerical models reproduced well the flexural cracks followed by the formation of an inclined crack that promotes the failure mechanism. However, some small differences shall also be highlighted (which are commonly neglected in most publications). While the cracking pattern of the test results of slender beams indicates an inclined crack with a convex/parabolic shape around the flexural cracks, the numerical models sometimes show inclined cracks with a more straight shape. In test S5A, this may explain the large difference in the failure loads observed. In practice, a parabolic cracking pattern disturbs the load transfer in the struts between the load and the support so that arching action cannot develop. Therefore, it is reasonable that the failure load in the numerical model from S5A has achieved a larger value than the experimental one.

Fig. 11 shows that, as in the experimental program, the numerical models started to fail by punching shear when the slab width increased to 2.5 m. At this point, notable differences between the cracking pattern

Fig. 10 also shows that the crack patterns from the test results were

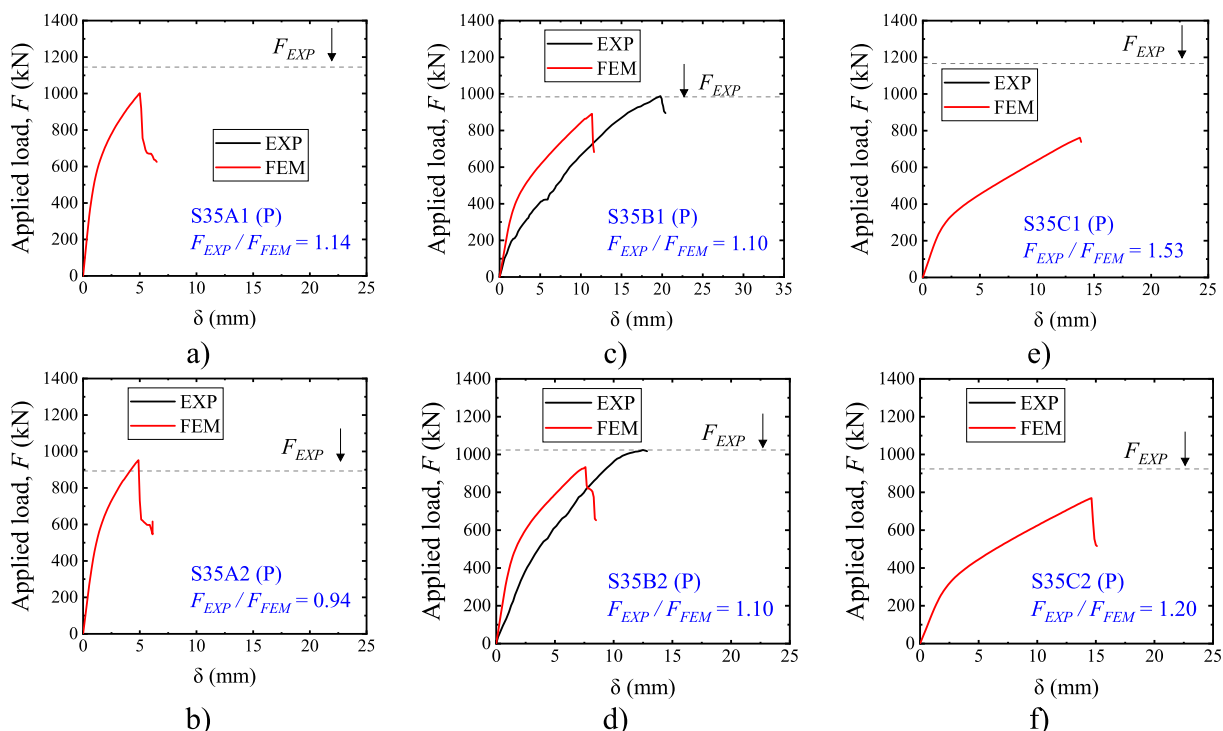


Fig. 12. Comparison between numerical and experimental results for the tests a) S35A-1; b) S35A-2; c) S35B-1; d) S35B-2; e) S35C-1; f) S35C-2.

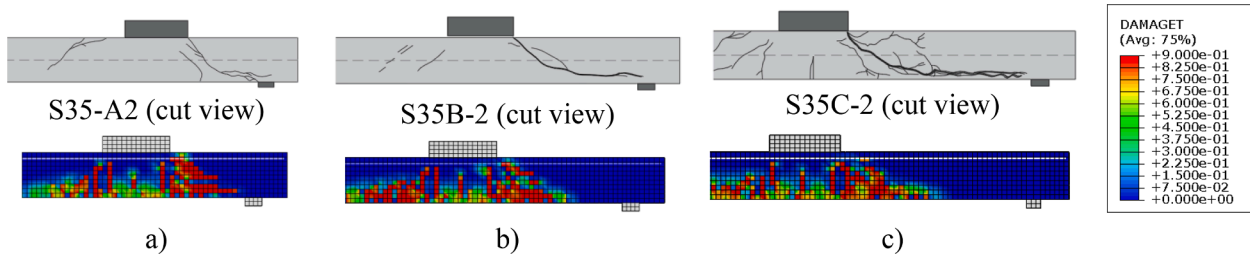


Fig. 13. Comparison between the FE models and the test results in terms of the cracking pattern for a) S35A-2, b) S35B-2, and c) S35C-2. Note: DAMAGET is the damage variable in tension.

Table 7
Summary of the predictions of ultimate capacity with the proposed approach for different subsets.

| Test | Failure mechanism | a_v/d_l [-] | a/d_l [-] | b_{slab}/l_{load} [-] | F_{EXP} / F_{FEM} [-] |
|--|-------------------|---------------|-------------|-------------------------|-------------------------|
| S5A | WB = shear | 1.91 | 2.91 | 1.25 | 0.63 |
| S5B-1 | WB = shear | 3.13 | 4.17 | 1.25 | 0.92 |
| S5B-2 | WB = shear | 3.13 | 4.17 | 1.25 | 0.92 |
| S15B-1 | WB = shear | 3.13 | 4.17 | 3.75 | 1.18 |
| S15B-2 | WB = shear | 3.13 | 4.17 | 3.75 | 1.24 |
| S25B-1 | P = Punching | 3.13 | 4.17 | 6.25 | 0.97 |
| S25B-2 | P = Punching | 3.13 | 4.17 | 6.25 | 1.06 |
| S35A-1 | P = Punching | 1.91 | 2.91 | 8.75 | 1.14 |
| S35A-2 | P = Punching | 1.91 | 2.91 | 8.75 | 0.94 |
| S35B-1 | P = Punching | 3.13 | 4.17 | 8.75 | 1.10 |
| S35B-2 | P = Punching | 3.13 | 4.17 | 8.75 | 1.10 |
| S35C-1 | P = Punching | 4.375 | 5.42 | 8.75 | 1.55 |
| S35C-2 | P = Punching | 4.375 | 5.42 | 8.75 | 1.20 |
| All tests | | | | AVG (COV) | 1.07 (20%) |
| All - S5A, S35C1 | | | | AVG (COV) | 1.07 (11%) |
| WB: S5B-1; S5B-2; S15B1; S15B-2 | | | | AVG (COV) | 1.06 (16%) |
| P: S25(B1,B2); S35(A1; A2; B1; B2; C2) | | | | AVG (COV) | 1.07 (9%) |

of the tests S15B-1 and S25B-1 appear: (i) the inclined crack visible on the side views from test S15B-1 does not appear in the test S25B-1 at failure; (ii) the inclined crack in the test S25B-1 develops only in the

Table 8
Comparison between tested and predicted resistances considering or not considering the damage parameters in the simulations.

| Comparison | | | | | With damage parameters | Without damage parameters | |
|------------------|-------------------------------------|---------------|-------------|-------------------------|-------------------------|---------------------------|--------------|
| Test | Failure mechanism | a_v/d_l [-] | a/d_l [-] | b_{slab}/l_{load} [-] | F_{EXP} / F_{FEM} [-] | F_{EXP} / F_{FEM} [-] | $\Delta(\%)$ |
| S5A | WB = shear | 1.91 | 2.91 | 1.25 | 0.63 | 0.60 | -5% |
| S5B-1 | WB = shear | 3.13 | 4.17 | 1.25 | 0.92 | 0.85 | -7% |
| S5B-2 | WB = shear | 3.13 | 4.17 | 1.25 | 0.92 | 0.90 | -3% |
| S15B-1 | WB = shear | 3.13 | 4.17 | 3.75 | 1.18 | 1.15 | -3% |
| S15B-2 | WB = shear | 3.13 | 4.17 | 3.75 | 1.24 | 1.17 | -5% |
| S25B-1 | P = Punching | 3.13 | 4.17 | 6.25 | 0.97 | 0.87 | -10% |
| S25B-2 | P = Punching | 3.13 | 4.17 | 6.25 | 1.06 | 0.95 | -11% |
| S35A-1 | P = Punching | 1.91 | 2.91 | 8.75 | 1.14 | 1.09 | -4% |
| S35A-2 | P = Punching | 1.91 | 2.91 | 8.75 | 0.94 | 0.89 | -5% |
| S35B-1 | P = Punching | 3.13 | 4.17 | 8.75 | 1.10 | 1.05 | -4% |
| S35B-2 | P = Punching | 3.13 | 4.17 | 8.75 | 1.10 | 1.06 | -4% |
| S35C-1 | P = Punching | 4.375 | 5.42 | 8.75 | 1.55 | 1.39 | -10% |
| S35C-2 | P = Punching | 4.375 | 5.42 | 8.75 | 1.20 | 1.16 | -4% |
| All tests | | | | AVG | 1.07 (20%) | 1.01 (19%) | -6% |
| All - S5A, S35C1 | | | | AVG | 1.07 (11%) | 1.01 (12%) | -5% |
| WB | S5B-1; S5B-2; S15B1; S15B-2 | | | AVG | 1.06 (16%) | 1.02 (16%) | -4% |
| P | S25(B1,B2); S35(A1; A2; B1; B2; C2) | | | AVG | 1.07 (9%) | 1.01 (11%) | -6% |

vicinity of the load, visible though cut views (typical from punching failures); (iii) the shape of the cracks from S15B-1 and S25B-1 are significantly different: while the test S15B-1 develops an inclined crack that connects different flexure cracks, the inclined crack in the test S25B-1 arises within a strut region around the load.

5.2. Accuracy level of the NLFEA according to the shear span for the wider slabs ($b_{slab} = 3.5$ m)

Fig. 12 shows the load \times displacement graphs of the numerical models and the ultimate load capacity of the tests (horizontal dashed lines - F_{EXP}). The tested load \times displacement graph of most tests was not reported in the references for such group [8]. Consequently, only a horizontal dashed line was added to represent the test's maximum achieved load F_{EXP} . Fig. 12 shows that the numerical model predicted well the ultimate capacity from most test results when varying the shear span, except for the test S35C-1 ($a/d_l = 5.4$).

Fig. 13 also shows that the punching shear failure that took place in the tests was well represented by the numerical models. Due to the higher shear demand on one of the sides of the load, an asymmetrical punching cone appeared in some tests. This characteristic was also well represented in the numerical models based on the higher concentration of tensile damage (DAMAGET) between the load and the support.

5.3. Summary of the level of accuracy with the proposed approach

Table 7 summarizes the relationship between the tested and predicted concentrated loads using the proposed approach for NLFEA. Different subsets were organized, removing and not removing outliers identified in the predictions. Besides, subsets were organized to highlight the results according to the governing failure mechanism (wide beams shear = WB and punching shear = P).

Table 7 shows that the average ratio between tested and predicted

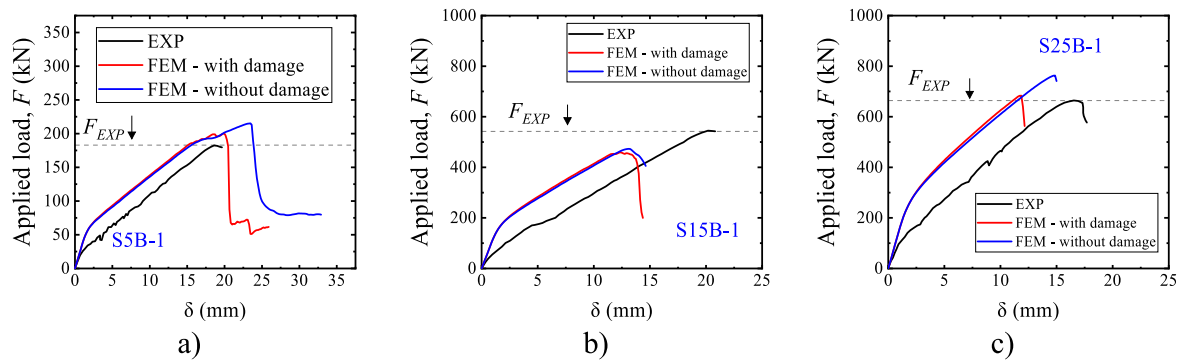


Fig. 14. Influence of including or not the damage parameters in the load × displacement curves of the numerical simulations. Note: graphs from other tests can be consulted in the Appendix.

applied loads at failure (F_{EXP}/F_{FEM}) was 1.07, with a coefficient of variation of only 20%. Since no particular calibration of the fracture energy or dilation angle was performed for every single test (the values used followed the same values and expressions for all tests), this level of precision was satisfactory. Removing the outliers S5A and S35C-1, the coefficient of variation decreases to 11%, which highlights the excellent precision of the proposed approach.

By organizing two subsets according to the governing failure mechanism, it can be seen that the level of precision was very similar for both failure mechanisms (WB and P). The average ratio between tested and predicted loads F_{EXP}/F_{FEM} was 1.06, with a coefficient of variation of 16% for the tests that failed as wide beams (WB). In turn, the tests that presented a punching failure (P) presented an average ratio F_{EXP}/F_{FEM} of 1.07 with a coefficient of variation of 9%. Therefore, a lower scatter was identified for the tests that failed by punching.

6. Sensitivity analysis

6.1. Effect of concrete damage evolution

Table 8 compares tested and predicted resistances with the FEM by considering and not considering the damage evaluation laws in the simulations. In general, it was observed that the predictions of ultimate capacity become less conservative without including the damage parameters. In other words, it was observed that the ultimate capacity predicted with the FEM decreased for all tests by including the damage parameters. In Table 8, the ratio F_{EXP}/F_{FEM} varied between 3% and 11% by including the damage parameters. In practice, the same level of

variation was observed regardless of the governing failure mechanism being wide beam shear (WB) or punching (P). Since both approaches (including and not including the damage parameters) led to similar levels of accuracy, it can be stated that the simulations could be performed without the damage parameters for simplicity.

Fig. 14 shows the load–displacement graph of some simulations with and without the damage parameters. Sometimes, including the damage parameters influenced only marginally the ultimate load and deformation capacity of some tests (S15B-1, for instance). Besides, Fig. 14 shows that in most cases, the brittle failure mechanism of the slabs was well represented with and without the damage parameters. This brittle mechanism is mainly related to the sharp decrease of the applied load at failure in the numerical simulations.

These similar results are explained in the following way. As demonstrated in Section 2, the effective uniaxial stress–strain behavior in compression and tension does not change, regardless of the damage parameters. In practice, including or not the damage parameters changes only the proportion between plastic and inelastic strains. Since cracks are not expected to close during the static tests (different from cyclic tests), such changes in the proportion between plastic and inelastic strains do not play a significant role in the numerical results. Nevertheless, the results with including damage parameters change slightly (between 3% and 11% in this study) because the difference in the evolution of plastic strain changes the evolution of effective stresses considered in the three-dimensional yield criterion from CDP [34,35].

Table 9

Comparison between tested and predicted resistances F_{EXP}/F_{FEM} according to the stress–strain behavior assumed in compression.

| Test | Failure mechanism | a_w/d_t [-] | a/d_t [-] | b_{stab}/l_{load} [-] | Stress–strain behavior in compression | | |
|--------------------------|---------------------------------|---------------|-------------|-------------------------|---|---|--|
| | | | | | EN 1992-1-1:2004 (Reference) F_{EXP} / F_{FEM} [-] | Carreira and Chu F_{EXP} / F_{FEM} [-] | Krätzig and Pölling F_{EXP} / F_{FEM} [-] |
| S5A | shear | 1.91 | 2.91 | 1.25 | 0.60 | 0.59 | 0.55 |
| S5B-1 | shear | 3.13 | 4.17 | 1.25 | 0.85 | 0.76 | 0.74 |
| S5B-2 | shear | 3.13 | 4.17 | 1.25 | 0.90 | 0.75 | 0.89 |
| S15B-1 | shear | 3.13 | 4.17 | 3.75 | 1.15 | 0.76 | 0.92 |
| S15B-2 | shear | 3.13 | 4.17 | 3.75 | 1.17 | 1.02 | 0.97 |
| S25B-1 | Punching | 3.13 | 4.17 | 6.25 | 0.87 | 0.82 | 0.85 |
| S25B-2 | Punching | 3.13 | 4.17 | 6.25 | 0.95 | 0.90 | 0.87 |
| S35A-1 | Punching | 1.91 | 2.91 | 8.75 | 1.09 | 1.10 | 1.07 |
| S35A-2 | Punching | 1.91 | 2.91 | 8.75 | 0.89 | 0.89 | 0.89 |
| S35B-1 | Punching | 3.13 | 4.17 | 8.75 | 1.05 | 1.16 | 1.04 |
| S35B-2 | Punching | 3.13 | 4.17 | 8.75 | 1.06 | 1.00 | 1.01 |
| S35C-1 | Punching | 4.375 | 5.42 | 8.75 | 1.39 | 1.31 | 1.24 |
| S35C-2 | Punching | 4.375 | 5.42 | 8.75 | 1.16 | 1.08 | 1.02 |
| All tests | | | | AVG (COV) | 1.01 (19%) | 0.93 (19%) | 0.93 (14%) |
| All tests (-) S5A, S35C1 | | | | AVG (COV) | 1.01 (12%) | 0.93 (16%) | 0.93 (10%) |
| WB | S5B-1; S5B-2; S15B1; S15B-2 | | | AVG (COV) | 1.02 (16%) | 0.82 (16%) | 0.88 (11%) |
| P | S25B1-2; S35A-1; A2; B1; B2; C2 | | | AVG (COV) | 1.01 (11%) | 0.99 (13%) | 0.96 (9%) |

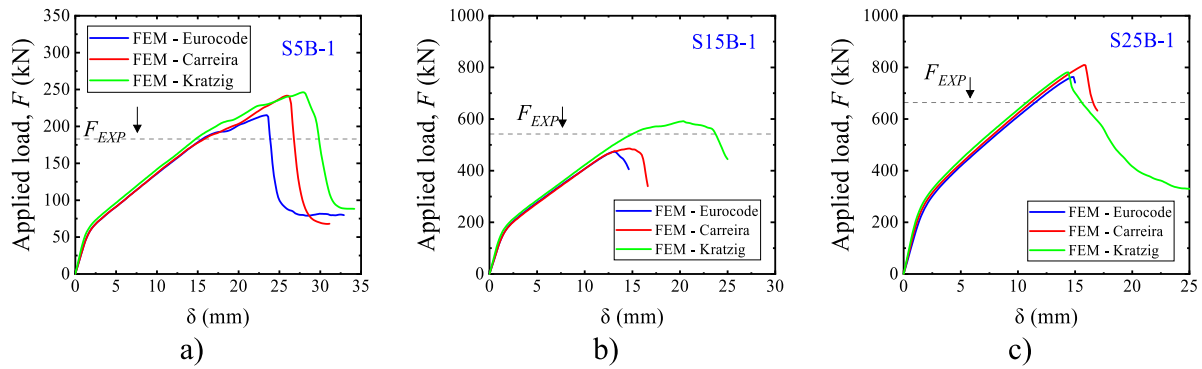


Fig. 15. Influence of the stress–strain behavior in compression assumed for the concrete. Note: graphs from other tests can be consulted in the Appendix.

Table 10

Comparison between tested and predicted resistances F_{EXP}/F_{FEM} according to the stress–strain behavior assumed in compression.

| Test | Failure mechanism | a_w/d_t [-] | a/d_t [-] | b_{slab}/l_{load} [-] | Stress–strain behavior in tension | | |
|--------------------------|---------------------------------|---------------|-------------|-------------------------|-----------------------------------|--|--------------|
| | | | | | Hordijk [31] (Reference) | | Δ (%) |
| | | | | | F_{EXP} / F_{FEM} [-] | Carreira and Chu [33] F_{EXP} / F_{FEM} [-] | |
| S5A | shear | 1.91 | 2.91 | 1.25 | 0.60 | 0.75 | 26% |
| S5B-1 | shear | 3.13 | 4.17 | 1.25 | 0.85 | 1.22 | 43% |
| S5B-2 | shear | 3.13 | 4.17 | 1.25 | 0.90 | 1.34 | 49% |
| S15B-1 | shear | 3.13 | 4.17 | 3.75 | 1.15 | 1.27 | 10% |
| S15B-2 | shear | 3.13 | 4.17 | 3.75 | 1.17 | 1.47 | 25% |
| S25B-1 | Punching | 3.13 | 4.17 | 6.25 | 0.87 | 1.26 | 44% |
| S25B-2 | Punching | 3.13 | 4.17 | 6.25 | 0.95 | 1.33 | 41% |
| S35A-1 | Punching | 1.91 | 2.91 | 8.75 | 1.09 | 2.08 | 90% |
| S35A-2 | Punching | 1.91 | 2.91 | 8.75 | 0.89 | 1.44 | 61% |
| S35B-1 | Punching | 3.13 | 4.17 | 8.75 | 1.05 | 1.78 | 69% |
| S35B-2 | Punching | 3.13 | 4.17 | 8.75 | 1.06 | 1.69 | 60% |
| S35C-1 | Punching | 4.375 | 5.42 | 8.75 | 1.39 | 2.65 | 91% |
| S35C-2 | Punching | 4.375 | 5.42 | 8.75 | 1.16 | 1.66 | 43% |
| All tests | | | | AVG (COV) | 1.01 (19%) | 1.53 (30%) | |
| All tests (-) S5A, S35C1 | | | | AVG (COV) | 1.01 (12%) | 1.50 (18%) | |
| WB | S5B-1; S5B-2; S15B1; S15B-2 | | | AVG (COV) | 1.02 (16%) | 1.32 (8%) | |
| P | S25B1-2; S35A-1; A2; B1; B2; C2 | | | AVG (COV) | 1.01 (11%) | 1.61 (18%) | |

6.2. Effect of the stress–strain behavior in compression

Table 9 shows the comparison between tested and predicted resistances with the FEM according to the different stress–strain behaviors in compression assumed to the concrete: EN 1992-1-1:2004 [28], Carreira and Chu [20] and Krätzig and Pölling [22]. In these analyses, the finite element models assume all properties of the reference finite element approach (Section 4), except that the damage parameters were not considered in these evaluations.

Table 9 shows that the accuracy of the different approaches is quite similar for slabs failing by punching (P). However, the predictions deviate by more than 12% compared to the reference approach considering only the tests that failed as wide beams in shear (WB). In practice, considering the large post-peak compressive strength according to the models from Carreira and Chu [20] and Krätzig and Pölling [22] overestimated the tested resistances in one-way shear. However, recalibrating other parameters, such as the fracture energy and dilation angle, these approaches may lead to almost the same results. Therefore, any of these models could be used since other secondary parameters can be properly calibrated.

Fig. 15 shows that, in general, the studied models changed only slightly the ultimate loads and the displacements at failure for most tests. The stress–strain models with a large residual compressive strength (Eurocode [28] < Carreira and Chu [20] < Krätzig and Pölling [22]) led, in most cases, to a higher ultimate load and deformation capacity at failure (test S5B1-1, for instance). In general, the governing failure mechanism was not changed by changing the stress–strain

behavior in compression. However, the tests S15B1- and S15B-2 showed that, in some cases, the use of the models from Carreira and Chu [20] and Krätzig and Pölling [22] might lead to less brittle failure mechanisms at failure (almost ductile for S15B-1). Therefore, it is necessary to evaluate more carefully the use of models that assume a large residual strength in compression.

6.3. Effect of the tensile stress–strain behavior

The assumed tensile stress–strain behavior for the CDP is frequently not discussed in depth in numerical studies. In general, this is one of the assumptions that varies more between different papers, which deserves a detailed analysis. Table 10 shows the influence of the two types of tensile stress–strain behavior models: (i) the one from Hordijk [31] is based on the tensile stress \times crack opening relationship, which depends on the tensile fracture energy G_f and the size of the finite element l_{eq} ; and (ii) the one from Carreira and Chu [33], is not dependent on the tensile fracture energy and mesh size.

Table 10 shows that the ratio between tested and predicted resistances F_{EXP} / F_{FEM} varies enormously with the assumed stress–strain behavior in tension. The average ratio F_{EXP} / F_{FEM} varied from 1.01 to 1.53, and the coefficient of variation varied from 19% to 30% when replacing the Hordijk model [31] with the Carreira and Chu model [33]. The ratio of F_{EXP} / F_{FEM} between the two approaches varied between 10% and 91% using the Hordijk [31] and Carreira and Chu [33] models. The larger deviations in the predictions with the models from Carreira and Chu [33] occurred for the tests that failed by punching (P). This

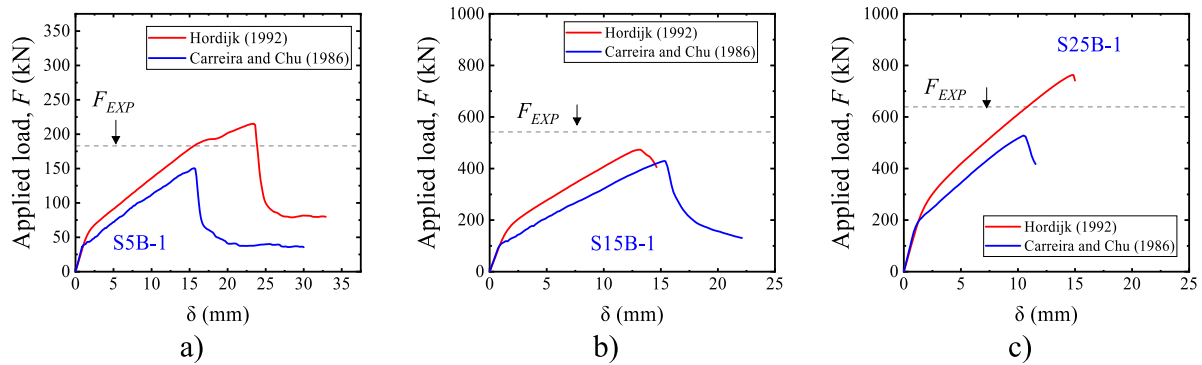


Fig. 16. Influence of the tensile stress–strain behavior. Note: graphs from other tests can be consulted in the Appendix.

Table 11

Comparison between tested and predicted resistances F_{EXP}/F_{FEM} according to the viscosity parameter μ .

| #1 | #2 | #3 | #4 | #5 | #6 | #7 | #8 | #9 |
|--------------------------|---------------------------------|---------------|-------------|-------------------------|---|--|--|--|
| Test | Failure mechanism | a_s/d_t [-] | a/d_t [-] | b_{slab}/l_{load} [-] | Viscosity parameter μ (Reference) $\mu = 10^{-3}$ $E_c = E_{cm}$ F_{EXP} / F_{FEM} [-] | (Reference) $\mu = 10^{-5}$ $E_c = E_{c,sec,pred}$ F_{EXP} / F_{FEM} [-] | $\mu = 10^{-4}$ $E_c = E_{c,sec,pred}$ F_{EXP} / F_{FEM} [-] | $\mu = 10^{-3}$ $E_c = E_{c,sec,pred}$ F_{EXP} / F_{FEM} [-] |
| S5A | shear | 1.91 | 2.91 | 1.25 | 0.63 | 0.62 | 0.54 | 0.42 |
| S5B-1 | shear | 3.13 | 4.17 | 1.25 | 0.92 | 0.85 | 0.80 | 0.58 |
| S5B-2 | shear | 3.13 | 4.17 | 1.25 | 0.92 | 1.07 | 0.90 | 0.62 |
| S15B-1 | shear | 3.13 | 4.17 | 3.75 | 1.18 | 1.05 | 0.95 | 0.68 |
| S15B-2 | shear | 3.13 | 4.17 | 3.75 | 1.24 | 1.10 | 0.98 | 0.70 |
| S25B-1 | Punching | 3.13 | 4.17 | 6.25 | 0.97 | 0.94 | 0.87 | 0.68 |
| S25B-2 | Punching | 3.13 | 4.17 | 6.25 | 1.06 | 0.97 | 0.93 | 0.71 |
| S35A-1 | Punching | 1.91 | 2.91 | 8.75 | 1.14 | 1.16 | 1.07 | 0.77 |
| S35A-2 | Punching | 1.91 | 2.91 | 8.75 | 0.94 | 0.89 | 0.85 | 0.63 |
| S35B-1 | Punching | 3.13 | 4.17 | 8.75 | 1.10 | 1.13 | 1.07 | 0.81 |
| S35B-2 | Punching | 3.13 | 4.17 | 8.75 | 1.10 | 1.07 | 1.01 | 0.76 |
| S35C-1 | Punching | 4.375 | 5.42 | 8.75 | 1.55 | 1.40 | 1.43 | 1.06 |
| S35C-2 | Punching | 4.375 | 5.42 | 8.75 | 1.20 | 1.21 | 1.14 | 0.90 |
| All tests | | | | AVG | 1.07 (20%) | 1.04 (18%) | 0.96 (21%) | 0.72 (22%) |
| All tests (-) S5A, S35C1 | | | | AVG | 1.07 (11%) | 1.04 (11%) | 0.96 (11%) | 0.71 (13%) |
| WB | S5B-1; S5B-2; S15B1; S15B-2 | | | AVG | 1.06 (16%) | 1.02 (11%) | 0.91 (9%) | 0.65 (8%) |
| P | S25B1-2; S35A-1; A2; B1; B2; C2 | | | AVG | 1.07 (9%) | 1.05 (11%) | 0.99 (11%) | 0.75 (12%) |

indicates that the punching shear mechanism is more dependent on the concrete tensile strength than the wide beam shear mechanism.

Fig. 16 shows how the assumed models to represent the concrete tensile behavior (Hordijk [31] and Carreira and Chu [33]) influence the load–displacement graphs of the simulations. The experimental curves were suppressed to highlight the influence of the parameter varied, keeping only the peak loads in the graphs. Besides showing the larger deviations in the peak loads, Fig. 16 shows that the model from Carreira and Chu [33] also results in lower concrete cracking loads of the slab (the inclination of the graphs that use the Carreira and Chu [33] model changes first).

6.4. Influence of the viscosity parameter and concrete elastic modulus

The scatter between tested and predicted values of the concrete elastic modulus E_c were relatively higher than the ones presented to the concrete tensile strength (coefficient of variation around 10% compared to < 1% in Table 5). Because of this, we compared the predictions of ultimate loads using the measured and predicted values of the concrete elastic modulus (Table 11, including damage parameters). Table 11 shows that, on average, the results were not significantly influenced using measured or predicted values of the concrete elastic modulus (comparing columns #6 and #7). The average ratio F_{EXP}/F_{FEM} changed

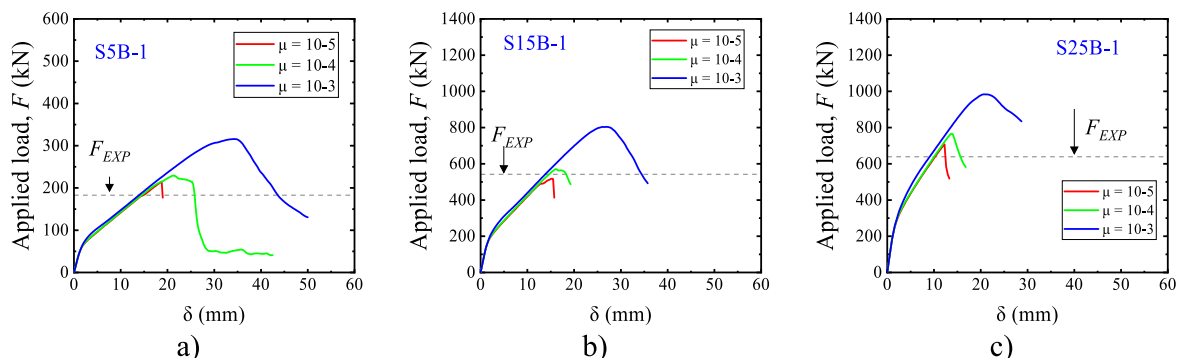


Fig. 17. Influence of the viscosity parameter value on the numerical results. Note: graphs from other tests can be consulted in the Appendix.

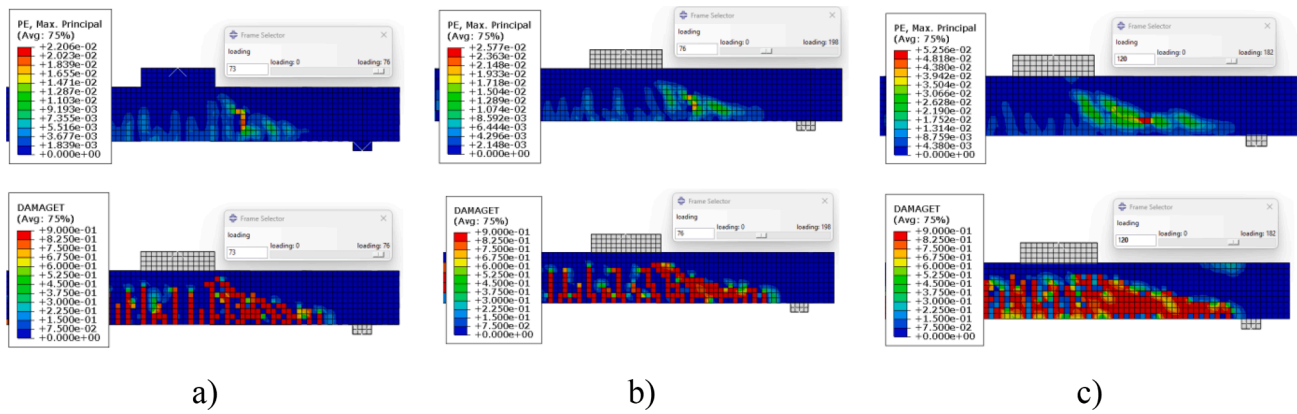


Fig. 18. Influence of the viscosity parameter μ on the distribution of plastic strains (PE,MAX PRINCIPAL) and tensile damage (DAMAGET) for the test S5B-1: a) $\mu = 10^{-5}$; b) $\mu = 10^{-4}$ and c) $\mu = 10^{-3}$.

Table 12
Modelling options proposed and from different approaches commonly found in the literature.

| Parameter | Approach (1) - Reference | Approach (2) | Approach (3) | Approach (4) |
|---------------------------------|--------------------------|-----------------------|-----------------------|-----------------------|
| $\sigma_c \times \varepsilon_c$ | EN 1992-1-1 [47] | Hognestad et al. [59] | Carreira and Chu [20] | Carreira and Chu [20] |
| $\sigma_t \times \varepsilon_t$ | Hordijk [31] | Petersson [29] | Carreira and Chu [33] | Carreira and Chu [33] |
| $d_c \times \varepsilon_c$ | - | - | - | - |
| $d_t \times \varepsilon_t$ | - | - | - | - |
| Fracture energy | Model Code 2010 | Model Code 1990 | - | - |
| Dilation angle | 30 | 40 | 40 | 40 |
| Viscosity | 0.00001 | 0.00001 | 0.001 | 0.00001 |
| Finite element | C3D8R | C3D8R | C3D8R | C3D8R |

from 1.07 using measured values to 1.04 using predicted values of E_c . Besides, the coefficient of variation changed from 20% to 18%. Therefore, in general, the results using the predicted concrete elastic modulus were slightly more precise.

Table 11 also shows the influence of the viscosity parameter value in the precision of the predictions of ultimate loads. The viscosity parameter values tested were 10^{-5} , 10^{-4} and 10^{-3} . Comparing columns #7, #8 and #9, it can be seen that increasing the values of the viscosity parameters increases the predicted ultimate loads (which resulted in this

Table 13
Comparison between tested and predicted resistances using the FEM based on different approaches (modeling options from Table 12). F.M. = failure mechanism.

| Test | F.M. | a_v/d_t [-] | a/d_t [-] | b_{slab}/l_{load} [-] | Approach 1 F_{EXP} / F_{FEM} [-] | Approach 2 F_{EXP} / F_{FEM} [-] | Approach 3 F_{EXP} / F_{FEM} [-] | Approach 4 F_{EXP} / F_{FEM} [-] |
|--------------------------|---------------------------------|---------------|-------------|-------------------------|---------------------------------------|---------------------------------------|---------------------------------------|---------------------------------------|
| S5A | shear | 1.91 | 2.91 | 1.25 | 0.60 | 0.55 | 0.36 | 0.63 |
| S5B-1 | shear | 3.13 | 4.17 | 1.25 | 0.85 | 0.73 | 0.52 | 1.32 |
| S5B-2 | shear | 3.13 | 4.17 | 1.25 | 0.90 | 0.71 | 0.54 | 1.22 |
| S15B-1 | shear | 3.13 | 4.17 | 3.75 | 1.15 | 0.95 | 0.51 | 1.18 |
| S15B-2 | shear | 3.13 | 4.17 | 3.75 | 1.17 | 1.01 | 0.51 | 1.30 |
| S25B-1 | Punching | 3.13 | 4.17 | 6.25 | 0.87 | 0.87 | 0.40 | 1.02 |
| S25B-2 | Punching | 3.13 | 4.17 | 6.25 | 0.95 | 0.92 | 0.43 | 1.08 |
| S35A-1 | Punching | 1.91 | 2.91 | 8.75 | 1.09 | 1.07 | 0.49 | 1.51 |
| S35A-2 | Punching | 1.91 | 2.91 | 8.75 | 0.89 | 0.89 | 0.37 | 1.43 |
| S35B-1 | Punching | 3.13 | 4.17 | 8.75 | 1.05 | 1.02 | 0.53 | 1.51 |
| S35B-2 | Punching | 3.13 | 4.17 | 8.75 | 1.06 | 0.95 | 0.51 | 1.43 |
| S35C-1 | Punching | 4.375 | 5.42 | 8.75 | 1.39 | 1.20 | 0.74 | 2.21 |
| S35C-2 | Punching | 4.375 | 5.42 | 8.75 | 1.16 | 1.07 | 0.56 | 1.30 |
| All tests | | | | AVG | 1.01 (19%) | 0.92 (19%) | 0.50 (20%) | 1.32 (27%) |
| All tests (-) S5A, S35C1 | | | | AVG | 1.01 (12%) | 0.93 (13%) | 0.49 (12%) | 1.30 (13%) |
| WB | S5B-1; S5B-2; S15B1; S15B-2 | | | AVG | 1.02 (16%) | 0.85 (18%) | 0.52 (2%) | 1.25 (5%) |
| P | S25B1-2; S35A-1; A2; B1; B2; C2 | | | AVG | 1.01 (11%) | 0.97 (9%) | 0.47 (15%) | 1.32 (15%) |

case on overestimated predictions of resistance in most cases). Increasing μ from 10^{-5} to 10^{-4} slightly changed the average ratio F_{EXP}/F_{FEM} from 1.08 to 0.96 (12.5% of change), while the coefficient of variation varied from 18% to 21%. However, increasing the viscosity parameter from 10^{-4} to 10^{-3} changed the average ratio F_{EXP}/F_{FEM} from 0.96 to 0.72 (33% of change), while the coefficient of variation remained similar.

Fig. 17 shows the influence of the viscosity parameter on the load \times displacement graphs. Increasing the viscosity parameter from 10^{-5} to 10^{-4} slightly increased the peak loads and the inclination of the descending branch in the load \times displacement graphs. By increasing the viscosity parameter from 10^{-4} to 10^{-3} , the peak loads increased more significantly and, in some cases (S35C2), provided a less brittle failure mechanism.

The cracking pattern can also be studied in the choice of the viscosity parameter. For instance, Fig. 18 shows the influence of the viscosity parameter on the distribution of plastic strains and tensile damage for the test S5B-1 (whose distribution represents the cracking pattern in the numerical models). Fig. 18 shows that, in general, the cracking pattern did not change significantly using $\mu = 10^{-5}$ or $\mu = 10^{-4}$. However, using a viscosity equal to 10^{-3} makes the distribution of tensile damage more diffuse and less concentrated (different from what would be expected in shear failures). In practice, using higher viscosity values has the same effect of artificially increasing the residual tensile strength of the concrete [58], which explains why the cracks are less concentrated in the numerical models with $\mu = 10^{-3}$.

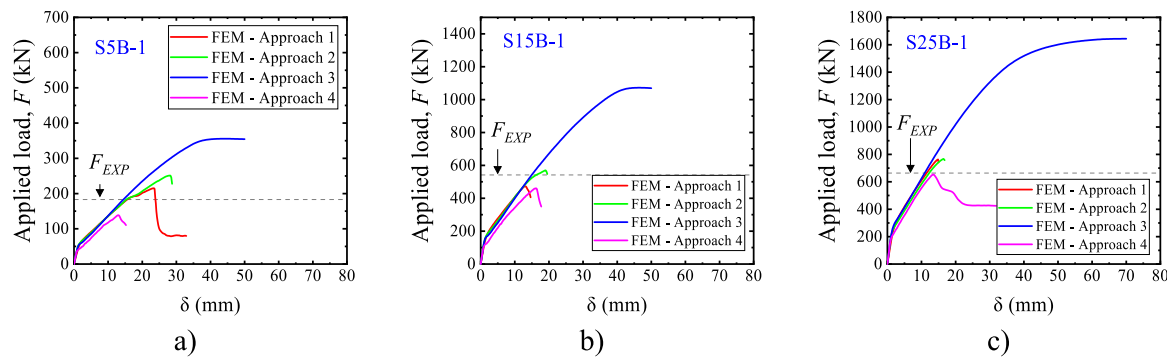


Fig. 19. Influence of different sets of modeling options (see Table 12) on load \times displacement graphs of the numerical models ($F \times \delta$). Note: graphs from other tests can be consulted in the Appendix.

6.5. Comparative analyses of different approaches from the literature

Table 12 describes four modeling approaches that combine different modeling options involving: (i) stress–strain behaviors in compression and tension, (ii) dilation angle values, (iii) fracture energy values, and (iv) viscosity parameters. Approach 1 is the proposed one (reference) in this study. Approach 2 is a modeling approach commonly found in studies related to punching capacity [13]. Approach 3 is one commonly used in studies related to composite structures [56]. In approach 3, the stress–strain behavior in tension [33] does not include the finite element size and, in general, the result is a significantly lower residual tensile strength after the peak stress compared to the models from Hordijk [31] and Petersson [29] (see Fig. 1b). Based only on the stress–strain behavior in tension, one could expect in this way a considerably lower ultimate capacity of the slabs considering Approach 3. Approach 4 is a modified approach from Approach 3, changing only the viscosity parameter. The damage parameters were not included in this section since it was observed that, in general, this parameter does not significantly change the global behavior of the numerical models in static problems.

Table 13 compares experimental and numerical failure loads using the different approaches (modeling options detailed in Table 12). Table 13 shows that even using significantly different values of fracture energy and dilation angle, approaches 1 and 2 led to similar levels of accuracy. In practice, this occurs because the higher fracture energy used in approach 1 is balanced with a lower dilation angle used. By comparing the predictions from approaches 1 and 2, higher differences occurred for the tests that failed in wide beam shear (WB), reaching differences between 10 and 20% in the predicted failure load. Conversely, the punching capacity predictions were very similar for both approaches.

On the other hand, approach 3 led to errors in the predicted failure load higher than 50%. All FEM predicted an overly unsafe failure load using approach 3, even though this approach is based on the use of a stress–strain behavior in tension with a considerably lower residual tensile strength after cracking. In practice, this occurred because the viscosity parameter used ($\mu = 0.001$) changed the effective stress–strain behavior in tension completely. In practice, a value higher than 0.0001 may change the material behavior to a perfect-plastic model [58]. Consequently, the material never fails in the concrete, and the slabs only fail after the reinforcement starts to yield.

In approach 4, the viscosity parameter from approach 3 was reduced to the value of 0.00001, which was demonstrated in other studies as being a value sufficiently low not to change the material behavior in an unpleasant way and allow numerical convergence in the processing of the FEM [14]. Table 13 shows that the predicted failure load decreased markedly from approach 3 to approach 4, and most of the prediction failure loads became on the safe side. In practice, the results from approach 4 become more conservative than the other approaches due to

the lower residual tensile strength after cracking. This occurs because the model from Carreira and Chu [33] to describe the stress–strain behavior in tension is not based on a stress–crack opening relationship and, hence, does not allow including the finite element size in the expressions. In general, approach 4 still led to large errors in the predicted failure load (>25%) for most tests and shall also be avoided.

Fig. 19 shows the influence of different sets of modeling options on load \times displacement graphs ($F \times \delta$) of the numerical models (see Table 12 for notations). From Fig. 19, the main observation is that beyond overestimating the failure load with approach 3, the failure mechanism of the slabs is also not represented by the numerical models. In practice, all numerical models presented a ductile failure mode using approach 3. Therefore, viscosity values should be carefully evaluated since they can introduce a large bias in the numerical results. In other words, when using large values of viscosity parameters, identifying different failure mechanisms of the slabs may become impossible.

7. Discussion

Available research in literature with recommendations for modeling experiments focuses on the idea that the NLFEA should be in agreement with the test results. However, some problems arise frequently in many studies: (i) the proposed approach is validated against one specific test; (ii) the limitations of the numerical model are not discussed or investigated; (iii) the material parameters are calibrated without considering their physical meaning. In this study, the accuracy of an arbitrary modeling approach was investigated to bring some light to the discussion.

When the numerical model is validated against one specific test, a severe problem may arise: (i) the proposed numerical model may have been validated against outlier test results and, hence it may not represent well most similar problems. For instance, if material parameters from the numerical model are calibrated to represent the test results of specimen S5A (as tested), the numerical model would not represent most test results well. In practice, the error of some numerical models increased to more than 50% when the modeling approach was changed to represent better the test S5A. Therefore, calibrating the numerical models using only one test specimen before applying the modeling strategy for a parametric study is not proper since it may reproduce inaccurate results.

Another main pitfall observed in several numerical studies is that the validation step from the study usually focuses on representing only one failure mechanism and does not cover all possible failure mechanisms that may arise in parametric studies. For instance, in the testing program performed by Reifßen, Classen and Hegger [8], it was identified that both one-way shear failure (as wide beams) and punching shear failure could occur by changing the slab's width. Therefore, this study could not include (by consistency) a variable such as a slab width in the parametric analyses if the numerical model is not validated to represent both failure

mechanisms.

In the context of NLFEA, it is also essential to understand the results of the outliers (numerical predictions that deviate overly from the test results). For instance, the difficulty of representing the failure load for test S5A is not coincidental. The failure load from non-slender beams (or wide slabs) is very sensitive to the cracking pattern that develops during the loading and the strut efficiency to transfer shear forces [60,61]. Consequently, a large scatter in the failure loads appears for such members, even when testing equal members. Therefore, it is more difficult for the numerical model to predict the correct failure load, as the failure mechanism to develop in the experiment and model is a matter of chance. In the case of test S35C-1, a similar interpretation occurs since the punching phenomenon also occurs in a region governed by strut and tie mechanisms (load vicinity) [62]. Since this test represents an asymmetrical punching in terms of load position and reinforcement ratios and no specific calibration was applied for each test, it would be natural that some predictions deviate more from the test results.

In many numerical studies, damage evolution parameters are not considered in the CDP model. The main argument is that the degradation of elastic stiffness would play a significant role only in cyclic loading tests, where the unloading would produce crack closing. However, an essential aspect of three-dimensional problems is neglected in this way: the degradation of the elastic modulus influences the triaxial state of concrete under confining problems. Since the yielding surface of the CDP model is pressure-sensitive, and the punching shear problems mobilize high confining stresses around the column, it can be expected that not including damage parameters could influence the numerical results. However, until now, no comprehensive investigation on this aspect has been conducted. This study showed that the failure load for shear and punching failure modes decreased between 3% and 11%, including the damage parameters. On average, the changes in the peak loads were less than 6%. Therefore, it can be stated that including or not including the damage parameters does not significantly influence the numerical results from static tests. In practice, for instance, decreasing the fracture energy G_f or the dilation angle ψ would provide similar results to that achieved by including the damage parameters but making the required number of input parameters lower.

One of the most common problems in numerical studies that consider the CDP model is the given value of the viscosity parameter. In practice, many researchers are tempted to use high values such as 0.001 and 0.0001 due to the lower processing time. In practice, increasing the viscosity parameter from 0.00001 to 0.001 may speed up the processing time more than 10 times (substantially decreasing the time required in the simulation). However, this choice has a cost that is not discussed in most papers. Depending on the value of μ , the concrete may behave as a perfectly plastic material in tension and compression. Michał and Andrzej [58] show that after a certain value of the viscosity parameter, the post-peak behavior of concrete under tension and compression changes very much, losing the descending branch in the stress-strain relationships expected for such materials. While this characteristic may have a minor influence on problems governed by flexure, using high values of viscosity parameters may induce flexural failures for all simulations (even when shear and punching failures are expected). Therefore, using high viscosity values when considering more than one failure mechanism (eg. concrete crushing, shear or punching) can be critical and should be avoided.

As demonstrated by Ungermaier et al. [63], the CDP and other constitutive models widely adopted in three-dimensional non-linear finite element analyses do not accurately represent the development of aggregate interlock (evolution of shear stresses between cracked faces). Although this shear transfer mechanism is well-known as a key parameter at shear failure, its influence in the numerical results may be limited due to the following reasons: (i) the contribution of aggregate interlock at failure, as well as other shear transfer mechanisms, depends on the location, geometry and kinematics of the critical shear crack and, hence,

in some case may have limited contribution to the shear capacity [64]; (ii) the contribution of aggregate interlock, in most cases, is significant (30% – 85%) only after the development of the second branch of the critical shear crack (CSC) around the compression chord, which usually happens close to the failure between (90% and 98% of the ultimate load) [65]; hence, inaccuracies in the evaluation of the aggregate interlock have more influence only at the last stage of the failure process; (iii) until the development of the second branch of the CSC around the compression chord and load levels around 90%, the compression chord capacity tends to be the most important shear transfer mechanism [4,66,67], which is well represented in most available constitutive models, including the CDP.

8. Recommendations for NLFEA using the CDP

In the last years, guidelines for NLFEA were developed that focused on using total strain fixed and rotating cracking models [68–73]. Nevertheless, the modeling choices using the Concrete Damaged Plasticity Model were not fully covered and were generally varied significantly between different publications [13,39,55,56]. In this study, we discussed the effect of these modeling choices of the CDP to predict the ultimate capacity of slabs failing in one-way shear and punching shear. Based on the presented analyses, the following recommendations can be stated:

- Damage parameters may be suppressed in the simulation of static tests for which shear and punching shear may be critical. Nevertheless, it's worth mentioning that the response of the numerical models based on fully elastoplastic materials tends to increase the ultimate loads between 3% and 11% compared to materials combining damage and plasticity parameters. In structural members associated with higher confining stresses, such as concrete-filled steel tubes, this level of influence may be higher, which requires further investigation.

- Any of the tested stress-strain behavior models in compression may be used in the simulations with the concrete damage plasticity model since other parameters from the constitutive models are well-defined. Nevertheless, on average, using the model with higher post-peak compressive strength [22] resulted in ultimate capacities 8% higher in the numerical simulations than the ones using the Eurocode expressions [28].

- The stress-strain behavior models in tension shall be based on stress-crack opening relationships [29–32] and consider the finite element size to overcome the mesh sensitivity. The use of models not based on the stress-crack opening relationships tends to result in overly conservative predictions of ultimate capacity when shear failures are expected (see Fig. 16) and shall be avoided.

- In the absence of testing results, the concrete tensile strength and concrete elastic modulus can be predicted using the *fib* Model Code 2010 expressions [27] based on the concrete compressive strength.

- The viscosity parameter shall be chosen in such a way as not to change significantly the numerical results and not based on the best prediction of ultimate loads, for instance. In this study, it was observed that the viscosity parameter should be not higher than 10^{-4} in simulations involving shear and punching shear failures.

9. Conclusions

This study discusses the level of accuracy of the proposed approach to predict the ultimate capacity of slabs under concentrated loads aided by NLFEA. The limitations and advantages of the proposed approach are highlighted. Besides, a sensitivity study was performed to show the effect of modeling options, such as the stress-strain behavior in compression and tension and the effect of damage parameters in the simulation of static tests. The following conclusions can be drawn:

- The proposed NLFEA modeling choices accurately predict the ultimate capacity of slab strips and slabs under concentrated loads when

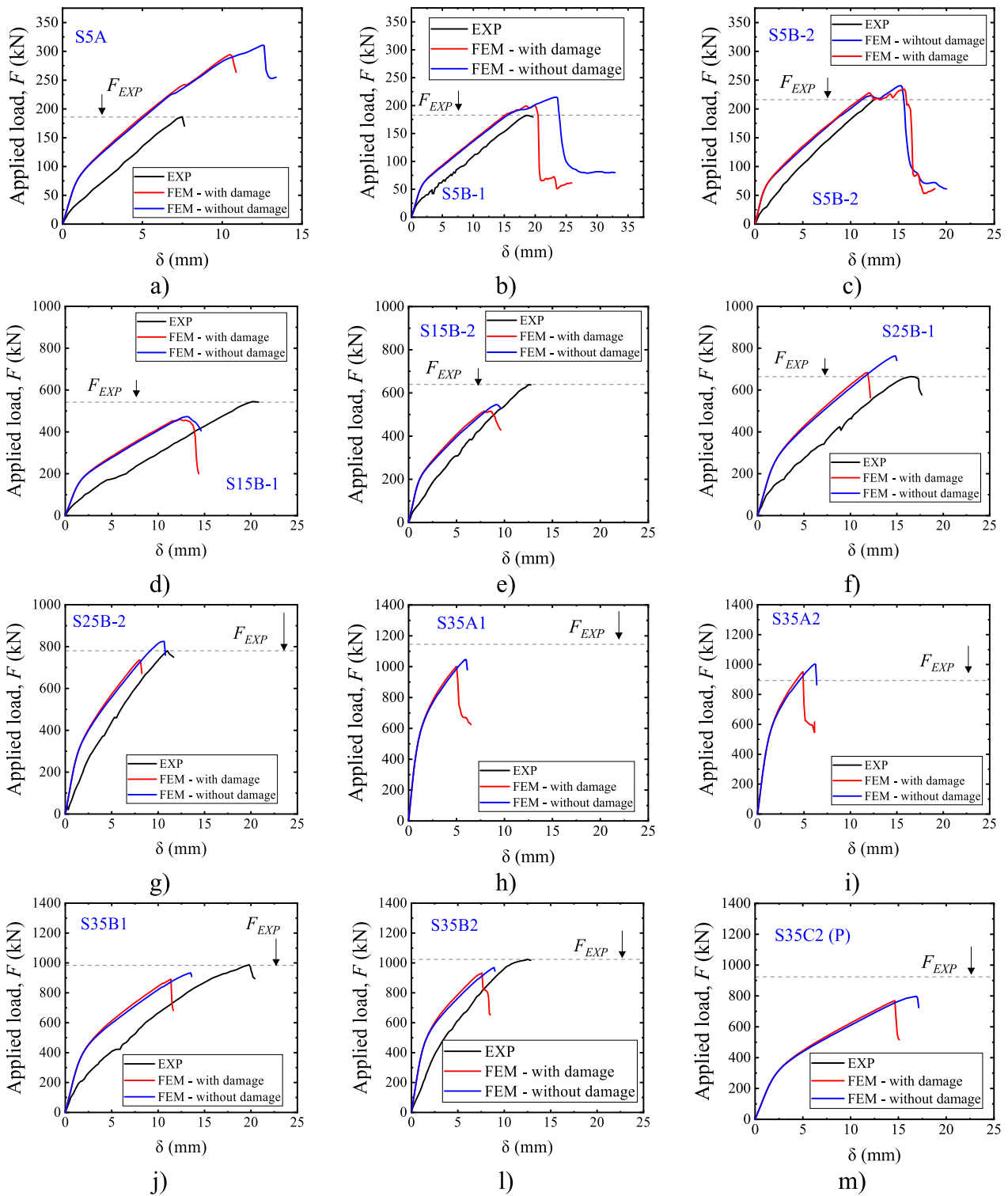


Fig. A1. Influence of including or not the damage parameters in the load × displacement curves of the numerical simulations.

the load is placed at distances $a_v > 2 d_t$. When the concentrated loads are placed closer to the support ($a_v < 2 d_t$), in some cases, the ultimate capacity is not predicted accurately because such tests are mostly influenced by the efficiency of the struts between the load and the support. Since there is a large scatter of experimental results for such loading conditions, it can be expected that the numerical models also have more difficulty in representing such failure mechanisms.

- Including the damage parameters in the NLFEA allows for representing more accurately the change in the confining stresses around the load at failure. However, it was found that the effect of including the damage parameters in static tests was limited for the evaluated tests. The variations in the predicted ultimate loads were in the order of 3% to 11%, including and not including the damage parameters. The failure mechanism of the tests did not change when not including the damage parameters. In practice, the tests' predicted

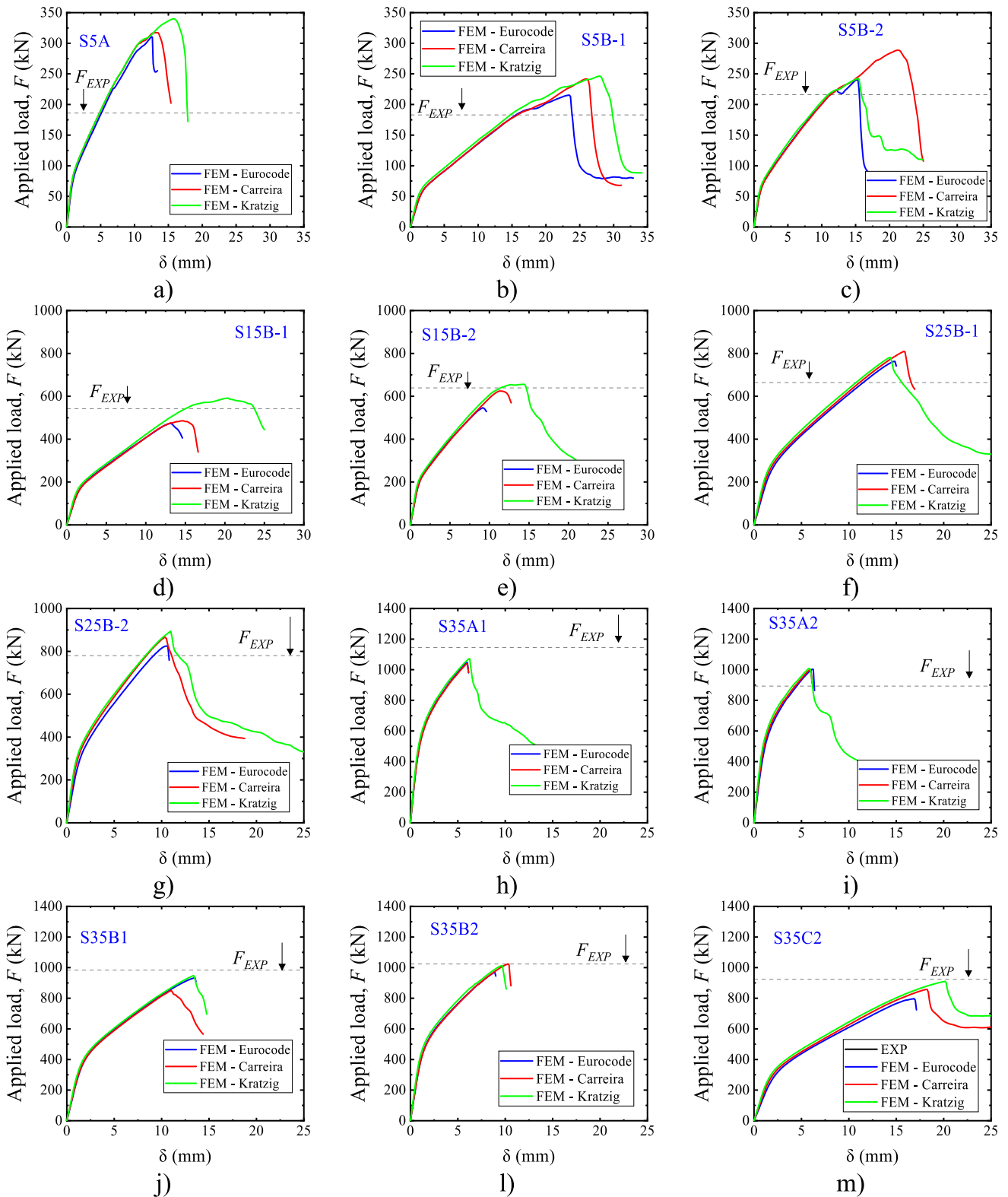


Fig. A2. Influence of the stress–strain behavior in compression assumed for the concrete.

ultimate load and deformation capacity decreased by including the damage parameters.

- The stress–strain behavior assumed in compression influences the ultimate capacity of wide beams and slab strips by around 10%. The influence of this parameter on the slabs that failed by punching was lower (around 5%). The assumed stress–strain behavior in

compression did not change the failure mechanism of the slabs. However, some tests presented a less brittle failure mechanism at the maximum load when using models with considerably higher residual compressive strength (for instance, Krätzig and Pölling [22]), which is an undesirable characteristic.

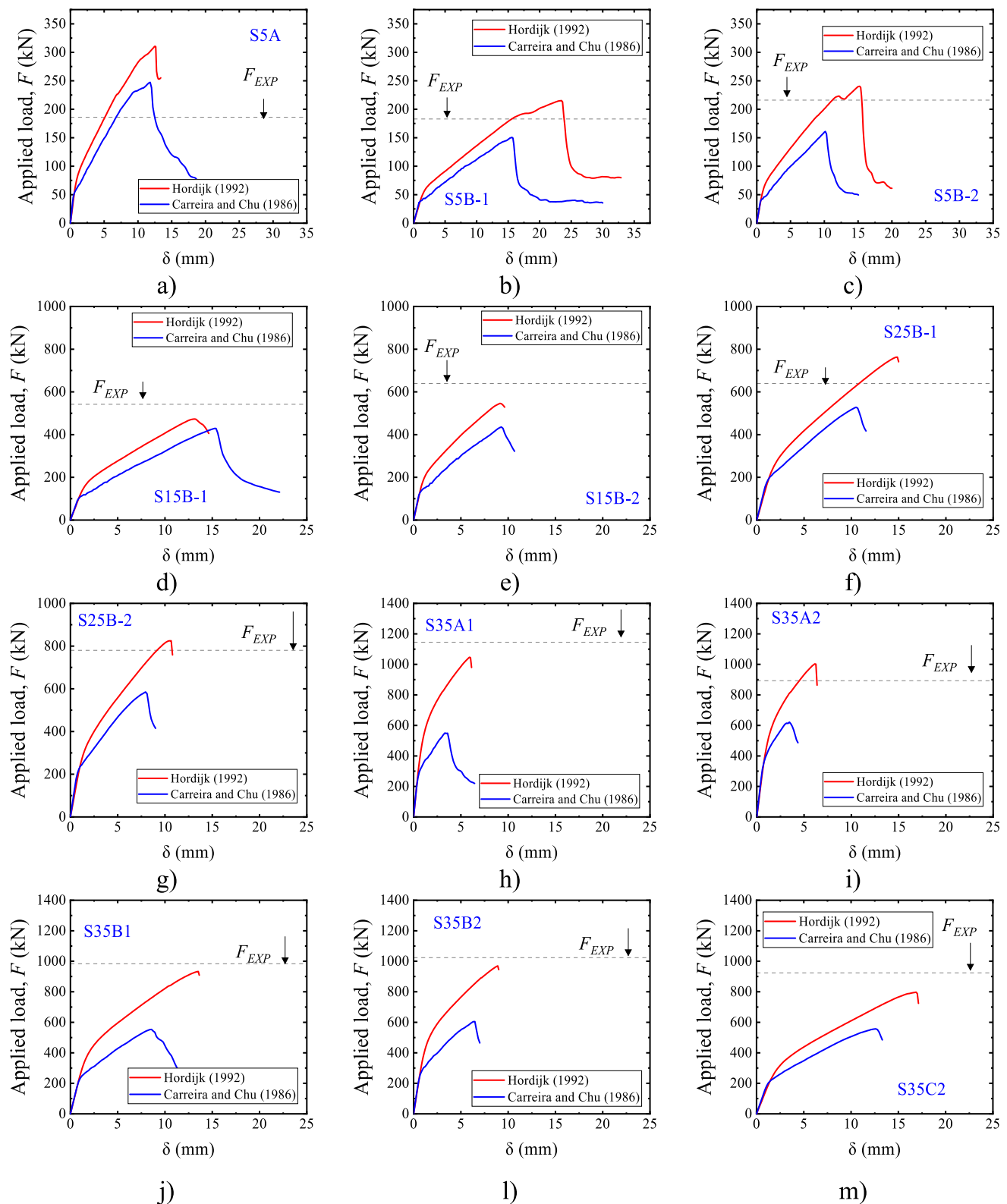


Fig. A3. Influence of the tensile stress–strain behavior.

- The use of large values of the viscosity parameter (for instance, 0.001) shall be avoided in NLFEA since these values change the effective material properties. In practice, the concrete may behave as perfectly plastic material; hence, the slabs' failure loads and mechanisms cannot be well represented. Even when flexural failure modes are well represented with large values of viscosity parameter, the

reader shall be aware that using such values introduces a large bias in the numerical results.

- Some modeling choices, even using considerably different values of fracture energy and dilation angle (stress–strain behavior under confining pressure), may lead to similar levels of accuracy for shear and punching shear capacity predictions. Nevertheless, other

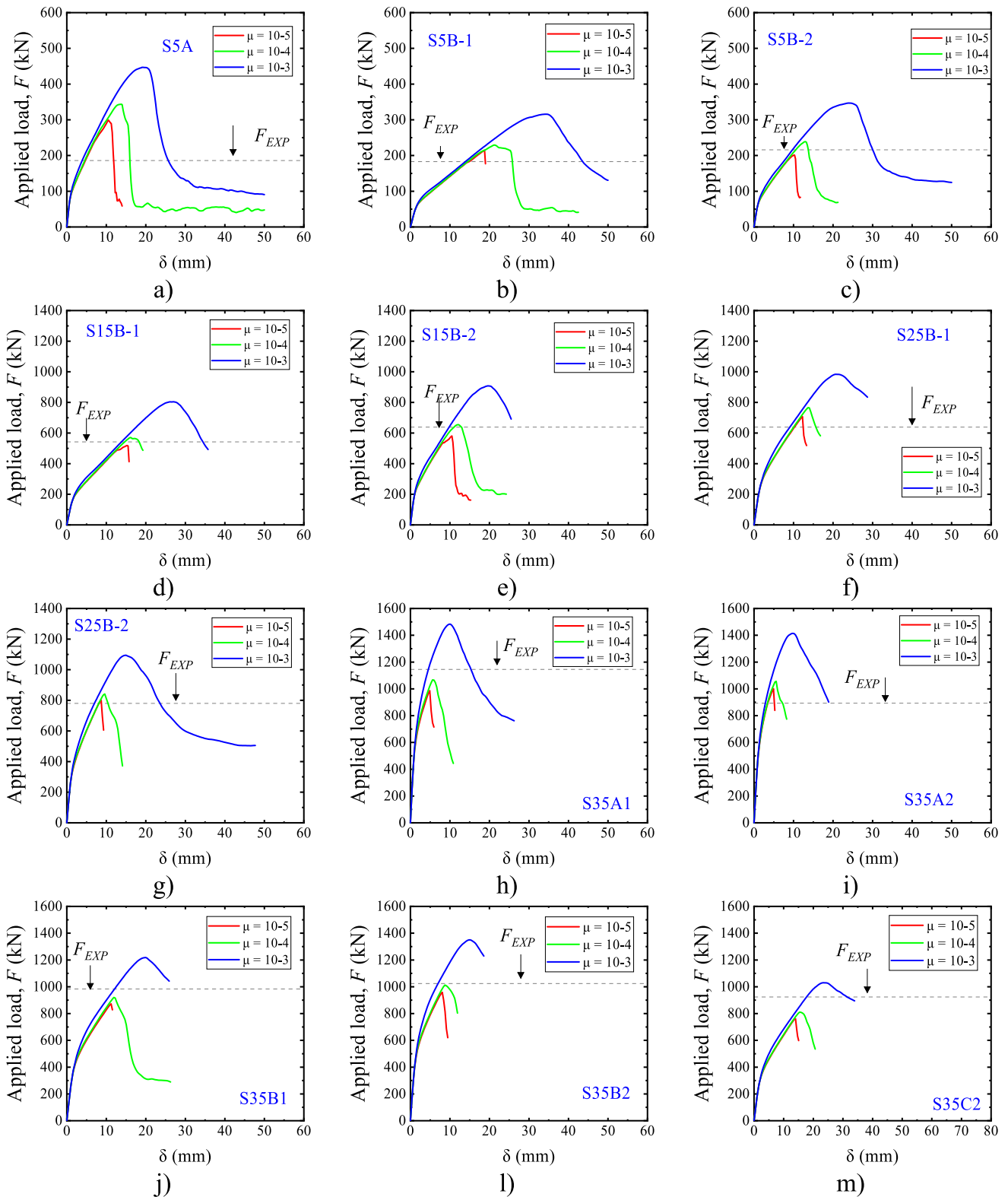


Fig. A4. Influence of the viscosity parameter value on the numerical results.

approaches that do not consider the mesh size in the stress–strain relationships for tension may provide unrealistic predictions of ultimate capacity and shall be avoided.

CRediT authorship contribution statement

Alex M.D. de Sousa: Conceptualization, Methodology, Resources, Data curation, Writing – original draft, Writing – review & editing. **Eva O.L. Lantsoght:** Conceptualization, Supervision, Writing – review & editing. **Aikaterini S. Genikomsou:** Methodology, Writing – review &

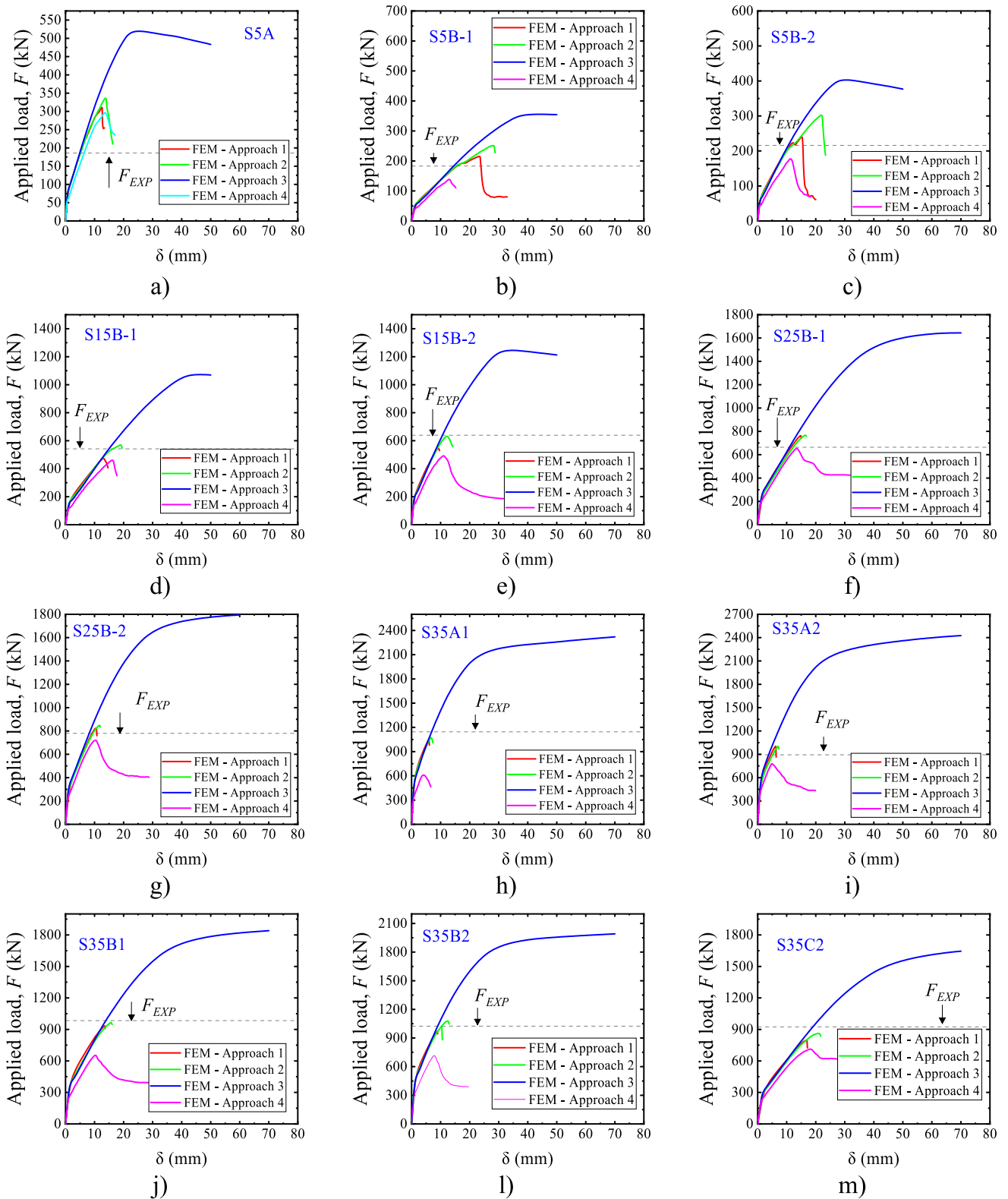


Fig. A5. Influence of different sets of modeling options (see Table 12) on load \times displacement graphs of the numerical models ($F \times \delta$).

editing. Lisiane P. Prado: Methodology, Writing – review & editing. Mounir K. El Debs: Supervision, Project administration, Funding acquisition.

Declaration of Competing Interest

The authors declare that they have no known competing financial interests or personal relationships that could have appeared to influence the work reported in this paper.

Data availability

Data will be made available on request.

Acknowledgements

The authors acknowledge the financial support provided by the Brazilian National Council for Scientific and Technological Development (CNPq, grant number 303438/2016-9) and the São Paulo Research Foundation (FAPESP, grant number #2018/21573-2, FAPESP grant number #2019/20092-3 and FAPESP grant number #2021/13916-0).

Appendix A

In this section, we present complementary graphs related to Section 6 (Sensitivity Analyses), including the load–displacement graphs from all tests simulated. Fig. A.1 describes the Influence of including or not the damage parameters in the load \times displacement curves of the numerical simulations. Fig. A.2 shows the influence of the stress–strain behavior in compression assumed for the concrete in the numerical results.

Fig. A.3 shows the influence of the different tensile stress–strain behavior models in the predictions. In the same context, Figure A. 4 describes the influence of the viscosity parameter value on the numerical results and Figure A. 5 detail the influence of different sets of modeling options (see Table 12) on load \times displacement graphs of the numerical models ($F \times \delta$). (Figs. A4 and A5).

References

- Lantsoght EOL, van der Veen C, Walraven JC. Shear in one-way slabs under concentrated load close to support. *ACI Struct J* 2013;110:275–84. <https://doi.org/10.14359/51684407>.
- Henze L, Rombach GA, Harter M. New approach for shear design of reinforced concrete slabs under concentrated loads based on tests and statistical analysis. *Eng Struct* 2020;219:110795. <https://doi.org/10.1016/j.engstruct.2020.110795>.
- Bui T-T, Limam A, Nana W-S-A, Ferrier E, Bost M, Bui Q-B. Evaluation of one-way shear behaviour of reinforced concrete slabs: experimental and numerical analysis. *Eur J Environ Civ Eng* 2020;24(2):190–216.
- Fernández PG, Marí A, Oller E. Theoretical prediction of the shear strength of reinforced concrete slabs under concentrated loads close to linear supports. *Struct Infrastruct Eng* 2023;19(7):890–903.
- de Sousa AMD, Lantsoght EOL, Yang Y, el Debs MK. Extended CSdT model for shear capacity assessments of bridge deck slabs. *Eng Struct* 2021;234:111897. <https://doi.org/10.1016/j.engstruct.2021.111897>.
- de Sousa AMD, Lantsoght EOL, Setiawan A, El Debs MK. Transition from one-way to two-way shear by coupling LEFEA and the CSCT models. Proceedings of the fib Symposium 2021, Concrete Structures: New Trends for Eco-Efficiency and Performance, Lisbon, Portugal: 2021.
- Lantsoght EOL, van der Veen C, de Boer A, Walraven JC. Influence of width on shear capacity of reinforced concrete members. *ACI Struct J* 2014;111:1441–9. <https://doi.org/10.14359/51687107>.
- Reißen K, Classen M, Hegger J. Shear in reinforced concrete slabs-Experimental investigations in the effective shear width of one-way slabs under concentrated loads and with different degrees of rotational restraint. *Struct Concr* 2018;19:36–48. <https://doi.org/10.1002/suco.201700067>.
- de Sousa AMD, Lantsoght EOL, el Debs MK. Shear and punching capacity predictions for one-way slabs under concentrated loads considering the transition between failure mechanisms. *Buildings* 2023;13:434. <https://doi.org/10.3390/buildings13020434>.
- de Sousa AMD, Lantsoght EOL, El Debs MK. Transition between shear and punching in RC SLABS: review and predictions with ACI code expressions. *ACI Struct J* 2023;120. <https://doi.org/10.14359/51738350>.
- Ribeiro PO, Gidrão GMS, Vareda LV, Carrazedo R, Malite M. Numerical and experimental study of concrete I-beam subjected to bending test with cyclic load. *Latin Am J Solids Struct* 2020;17:266. <https://doi.org/10.1590/1679-78255880>.
- Santos DP, Fernandes Neto JAD, Reginato L, Carrazedo R. Optimized design of RC deep beams based on performance metrics applied to strut and tie model and in-plane stress conditions. *Latin Am J Solids Struct* 2019;16:212. <https://doi.org/10.1590/1679-78255633>.
- Genikomsou AS, Polak MA. Finite element analysis of punching shear of concrete slabs using damaged plasticity model in ABAQUS. *Eng Struct* 2015;98:38–48. <https://doi.org/10.1016/j.engstruct.2015.04.016>.
- de Sousa AMD, Lantsoght EOL, Genikomsou AS, Krahl PA, El Debs MK. Behavior and punching capacity of flat slabs with the rational use of UHPFRC: NLFEA and analytical predictions. *Eng Struct* 2021;244:112774. <https://doi.org/10.1016/j.engstruct.2021.112774>.
- Reißen K. Zum Querkrafttragverhalten von einachsig gespannten Stahlbetonplatten ohne Querkraftbewehrung unter Einzellasten. Doctor of Engineering. PhD Thesis (Doctor of Engineering), Faculty of Civil Engineering, RWTH Aachen University, 2016.
- Henze L. Querkrafttragverhalten von Stahlbeton-Fahrbahnplatten. PhD Thesis, Institute for Concrete Structures, Technische Universität Hamburg (TUHH), 2019.
- Palhares R, Rossignoli F, Melo G, Lima H. A numerical model capable of accurately simulating the punching shear behavior of a reinforced concrete slab. *Struct Concr* 2022;23(2):1134–50.
- Tran NL. A mechanical model for the shear capacity of slender reinforced concrete members without shear reinforcement. *Eng Struct* 2020;219:110803. <https://doi.org/10.1016/j.engstruct.2020.110803>.
- Ravasini S, Vecchi F, Belletti B, Muttoni A. Verification of deflections and cracking of RC flat slabs with numerical and analytical approaches. *Eng Struct* 2023;284:115926. <https://doi.org/10.1016/j.engstruct.2023.115926>.
- Carreira DJ, Chu KH. Stress-strain relationship for plain concrete in compression. *ACI J* 1985;82(6):797–804.
- Guo Z. Principles of reinforced concrete design. principles of reinforced. *Concrete* 2014;587. <https://doi.org/https://doi.org/10.1016/B978-0-12-800859-1.00004-9>.
- Krätzig WB, Pölling R. An elasto-plastic damage model for reinforced concrete with minimum number of material parameters. *Comput Struct* 2004;82:1201–15. <https://doi.org/10.1016/J.COMPSTRUC.2004.03.002>.
- Hognestad E. Yield-line theory for the ultimate flexural strength of reinforced concrete slabs. *ACI J Proc* 1953;49:637–56. <https://doi.org/10.14359/11842>.
- Feenstra PH. Computational aspects of biaxial stress in plain and reinforced concrete. PhD Thesis, Delft University of Technology: Civil Engineering and Geosciences; 1993.
- Oller S. A continuous damage model for frictional materials (in spanish). Doctoral Dissertation. Doctoral Dissertation, Technical University of Catalonia; 1988.
- Comité Euro-International du Béton. CEB-FIP Model Code 1990: design code. 1993. <https://doi.org/10.1680/ceb-fipmcl1990.35430>.
- Fédération Internationale du Béton (fib). fib Model Code for Concrete Structures 2010. vol. 1–2. Lausanne, Switzerland: Ernst & Sohn - fédération internationale du béton, Bulletin 65; 2012.
- CEN. EN 1992-1-1: Eurocode 2: Design of concrete structures -Part 1-1: General rules and rules for buildings, EN 1992-1-1:2004 2004.
- Petersson P. Crack growth and development of fracture zones in plain concrete and similar materials. Division of Building Materials 1981:1–174. <https://doi.org/Division of Building Materials>.
- Cornelissen HAW, Hordijk DA, Reinhardt HW. Experimental determination of crack softening characteristics of normal weight and lightweight concrete. *Heron* 1986;31:45–56.
- Hordijk DA. Tensile and tensile fatigue behaviour of concrete — experiments, modelling and analyses. *Heron* 1992;37:3–79.
- Hillerborg A, Modéer M, Petersson P-E. Analysis of crack formation and crack growth in concrete by means of fracture mechanics and finite elements. *Cem Concr Res* 1976;6:773–81. [https://doi.org/10.1016/0008-8846\(76\)90007-7](https://doi.org/10.1016/0008-8846(76)90007-7).
- Carreira DJ, Chu KH. Stress-strain relationship for reinforced concrete in tension. *J Am Concr Inst* 1986;83:21–8. <https://doi.org/10.14359/1756>.
- Lublinter J, Oliver J, Oller S, Onate E. A plastic-damage model for concrete. *Int J Solids Struct* 1989;25:299–326. [https://doi.org/10.1016/0020-7683\(89\)90050-4](https://doi.org/10.1016/0020-7683(89)90050-4).
- Lee J, Fenves GL. Plastic-damage model for cyclic loading of concrete structures. *J Eng Mech* 1998;124:892–900. [https://doi.org/10.1061/\(ASCE\)0733-9399\(1998\)124:8\(892\)](https://doi.org/10.1061/(ASCE)0733-9399(1998)124:8(892)).
- Cheng H, Paz CM, Pinheiro BC, Estefen SF. Experimentally based parameters applied to concrete damage plasticity model for strain hardening cementitious composite in sandwich pipes. *Mater Struct/Materiaux et Constructions* 2020;53:1–17. <https://doi.org/10.1617/s11527-020-01513-9>.
- Birtel V, Mark P. Parameterised finite element modelling of RC beam shear failure. *Abaqus User's Conference* 2006:95–108.
- Yu T, Teng JG, Wong YL, Dong SL. Finite element modeling of confined concrete-I: Drucker-Prager type plasticity model. *Eng Struct* 2010;32:665–79. <https://doi.org/10.1016/J.ENGSTRUCT.2009.11.014>.
- Alfarah B, López-Almansa F, Oller S. New methodology for calculating damage variables evolution in plastic damage model for RC structures. *Eng Struct* 2017;132:70–86. <https://doi.org/10.1016/j.engstruct.2016.11.022>.
- Peter Mark. Zweiachsig durch Biegung und Querkräfte beanspruchte Stahlbetonträger. Schriftenreihe des Instituts für konstruktiven Ingenieurbau, Ruhr-Univ. Bochum, Heft 2006-3., 2006.
- Yu T, Teng JG, Wong YL, Dong SL. Finite element modeling of confined concrete-II: Plastic-damage model. *Eng Struct* 2010;32:680–91. <https://doi.org/10.1016/J.ENGSTRUCT.2009.11.013>.
- Dassault Systems Simulia Corp. Abaqus Analysis user's manual 6.14. Providence, Rhode Island (USA): Dassault Systems Simulia Corp.; 2014.
- Nana WSA, Bui TT, Limam A, Abouri S. Experimental and numerical modelling of shear behaviour of full-scale RC slabs under concentrated loads. *Structures* 2017;10:96–116. <https://doi.org/10.1016/j.istruc.2017.02.004>.
- Yan C, Shi Y, Li Z, Wen S, Wei Q. Numerical analysis of selective laser sintering key technology. *Select Laser Sint Addit Manuf Technol* 2021:713–872. <https://doi.org/10.1016/B978-0-08-102993-0.00006-0>.
- Santos JVC. Análise numérica de cálice de fundação em bloco sobre duas estacas. Universidade de São Paulo 2022. <https://doi.org/10.11606/D.18.2022.TDE-20122022-124144>.

- [46] Xenos D, Grassl P. Modelling the failure of reinforced concrete with nonlocal and crack band approaches using the damage-plasticity model CDPM2. *Finite Elem Anal Des* 2016;117–118:11–20. <https://doi.org/10.1016/J.FINEL.2016.04.002>.
- [47] CEN. EN 1992-1-1: Eurocode 2: Design of concrete structures -Part 1-1: General rules and rules for buildings, EN 1992-1-1:2005 2005.
- [48] Genikomsou AS, Polak MA. Finite-element analysis of reinforced concrete slabs with punching shear reinforcement. *J Struct Eng* 2016;142:1–15. [https://doi.org/10.1061/\(ASCE\)ST.1943-541X.0001603](https://doi.org/10.1061/(ASCE)ST.1943-541X.0001603).
- [49] Milligan GJ, Polak MA, Zurell C. Finite element analysis of punching shear behaviour of concrete slabs supported on rectangular columns. *Eng Struct* 2020; 224:111189. <https://doi.org/10.1016/j.engstruct.2020.111189>.
- [50] Milligan GJ, Polak MA, Zurell C. Impact of column rectangularity on punching shear strength: code predictions versus finite element analysis. *J Struct Eng* 2021; 147:04020331. [https://doi.org/10.1061/\(ASCE\)ST.1943-541X.0002889](https://doi.org/10.1061/(ASCE)ST.1943-541X.0002889).
- [51] Genikomsou AS, Polak MA. 3D finite element investigation of the compressive membrane action effect in reinforced concrete flat slabs. *Eng Struct* 2017;136: 233–44. <https://doi.org/10.1016/j.engstruct.2017.01.024>.
- [52] Poliotti M, Bairán J-M. A new concrete plastic-damage model with an evolutive dilatancy parameter. *Eng Struct* 2019;189:541–9. <https://doi.org/10.1016/J.ENGSTRUCT.2019.03.086>.
- [53] Kupfer H, Hilsdorf HK, Rusch H. Behavior of concrete under biaxial stresses. *ACI J Proc* 1969;66:656–66. <https://doi.org/10.14359/7388>.
- [54] Kupfer HB, Gerstle KH. Behavior of concrete under biaxial stresses. *J Eng Mech Div* 1973;99(4):853–66.
- [55] Aguiar A, Oliveira D, Reis L, Nzambi A. Punching shear strength of waffle flat slabs with opening adjacent to elongated columns. *Eng Struct* 2021;243:112641. <https://doi.org/10.1016/j.engstruct.2021.112641>.
- [56] Ferreira FPV, Martins CH, De Nardin S. Sensitivity analysis of composite cellular beams to constitutive material models and concrete fracture. *Int J Struct Stab Dyn* 2021;21(01):2150008.
- [57] Wosatko A, Winnicki A, Polak MA, Pamin J. Role of dilatancy angle in plasticity-based models of concrete. *Arch Civil Mech Eng* 2019;19:1268–83. <https://doi.org/10.1016/J.ACME.2019.07.003>.
- [58] Michal S, Andrzej W. Calibration of the CDP model parameters in Abaqus. The 2015 World Congress on Advances in Structural Engineering and Mechanics (ASEM15), Incheon, Korea; 2015.
- [59] Hognestad E, Hanson NW, McHenry D. Concrete stress distribution in ultimate strength design. *J Proc* 1955;52:455–80. <https://doi.org/10.14359/11609>.
- [60] Mihaylov BI, Bentz EC, Collins MP. Two-parameter kinematic theory for shear behavior of deep beams. *ACI Struct J* 2013;110:447–55. <https://doi.org/10.14359/51685602>.
- [61] Sousa AMD, Lantsoght EOL, El Debs MK. One-way shear strength of wide reinforced concrete members without stirrups. *Struct Concr* 2021;22(2):968–92.
- [62] Muttoni A, Fernandez Ruiz M. Shear in slabs and beams: should they be treated in the same way? *FIB Bulletin* 57: shear and punching shear in RC and FRC elements., 2010, p. 105–28.
- [63] Ungermann J, Adam V, Classen M. Fictitious rough crack model (FRCM): A smeared crack modelling approach to account for aggregate interlock and mixed mode fracture of plain concrete. *Materials* 2020;13:2774. <https://doi.org/10.3390/MA13122774>.
- [64] Cavagnis F, Fernández Ruiz M, Muttoni A. An analysis of the shear-transfer actions in reinforced concrete members without transverse reinforcement based on refined experimental measurements. *Struct Concr* 2018;19:49–64. <https://doi.org/10.1002/suco.201700145>.
- [65] Montoya-Coronado LA, Ribas C, Ruiz-Pinilla JG, Cladera A. Time-history analysis of aggregate interlock in reinforced concrete beams without stirrups. *Eng Struct* 2023;283:115912.
- [66] Cladera A, Marí A, Bairán JM, Ribas C, Oller E, Duarte N. The compression chord capacity model for the shear design and assessment of reinforced and prestressed concrete beams. *Struct Concr* 2016;17:1017–32. <https://doi.org/10.1002/suco.201500214>.
- [67] Bairán JM, Mendiña R, Marí A, Cladera A. Shear strength of non-slender reinforced concrete beams. *ACI Struct J* 2020;277–90. <https://doi.org/10.14359/51721369>.
- [68] RTD 1016-3C:2017. Validation of the Guidelines for Nonlinear Finite Element Analysis of Concrete Structures - Part: Slabs 2017.
- [69] Belletti B, Damoni C, Hendriks MAN. Development of guidelines for nonlinear finite element analyses of existing reinforced and pre-stressed beams. *Eur J Environ Civ Eng* 2011;15:1361–84. <https://doi.org/10.1080/19648189.2011.9714859>.
- [70] RTD 1016-3A:2017. Validation of the Guidelines for Nonlinear Finite Element Analysis of Concrete Structures - Part: Reinforced beams 2017.
- [71] Hendriks MAN, de Boer A, Belletti B. Guidelines for Nonlinear Finite Element Analysis of Concrete Structures. Rijkswaterstaat Technical Document (RTD), Report RTD: 1016-1:2017; 2017.
- [72] RTD 1016:2012. Guidelines for Nonlinear Finite Element Analysis of Concrete Structures - Scope: Girder Members 2012:65.
- [73] Díaz RS, Trautwein LM, de Almeida LC. Numerical investigation of the punching shear capacity of unbonded post-tensioned concrete flat slabs. *Struct Concr* 2020; 1–18. <https://doi.org/10.1002/suco.202000448>.